Integrated petrological and geophysical constraints on magma system architecture in the western Galápagos Archipelago: insights from Wolf volcano

Michael J. Stock[1*], Marco Bagnardi[2,3], David A. Neave[4], John Maclennan[1], Benjamin Bernard[5], Iris Buisman[1], Matthew L.M. Gleeson[1], Dennis Geist[6,7]

[1] Department of Earth Sciences, University of Cambridge, Cambridge, United Kingdom

[2] COMET, School of Earth and Environment, University of Leeds, Leeds, United Kingdom

[3] Now at: Jet Propulsion Laboratory, California Institute of Technology, Pasadena, CA, United States

[4] Leibniz Universität Hannover, Institut für Mineralogie, Callinstraße 3, 30167 Hannover, Germany

[5] Instituto Geofísico, Escuela Politécnica Nacional, Quito, Ecuador

[6] Department of Geology, Colgate University, Hamilton, NY, United States

[7] Division of Earth Sciences, U.S. National Science Foundation, Alexandria, VA, United States

*E-mail: ms2368@cam.ac.uk

Key points

- Combined geophysical and petrological constraints provide a detailed picture of the sub-volcanic architecture at Wolf volcano.
- Wolf is underlain by two discrete magma storage regions: one within the edifice, the other in the lower crust.
- Almost all the magma ejected during the 2015 eruption of Wolf was derived from the lower crust.

Abstract

The 2015 eruption of Wolf volcano was one of the largest eruptions in the Galápagos Islands since the onset of routine satellite-based volcano monitoring. It therefore provides an excellent opportunity to combine geophysical and petrological data, to place detailed constraints on the architecture and dynamics of sub-volcanic systems in the western archipelago. We present new geodetic models which show that pre-eruptive inflation at Wolf was caused by magma accumulation in a shallow flat-topped reservoir at ~1.1 km, whereas edifice-scale deformation during the eruption was related to a deflationary source at 6.1–8.8 km. Petrological observations suggest that the erupted material was derived from both a sub-volcanic mush and a liquid-rich magma body. Using a combination of olivine-plagioclase-augite-melt (OPAM) and clinopyroxene-melt barometry, we show that the majority of magma equilibration, crystallisation and mush entrainment occurred at a depth equal to or greater than the deep geodetic source, with little petrological evidence of material sourced from shallower levels. Hence, our multidisciplinary study does not support a fully trans-crustal magmatic system beneath Wolf volcano before the 2015 eruption, but instead indicates two discrete storage regions, with a small magma lens at shallow levels and the major zone of magma storage in the lower crust, from which most of the erupted material was sourced. A predominance of lower crustal magma storage has previously been thought typical of sub-volcanic systems in the eastern Galápagos Archipelago, but our new data suggest that this may also occur beneath the more active volcanoes of the western archipelago.

1. Introduction

Determining the crustal-scale architecture of magma plumbing systems is essential for understanding sub-volcanic processes, such as crystallisation, magma mixing, mush formation and assimilation, as well as recognising critical pre-eruptive 'warning' signs in volcano monitoring data. Before and during eruptions, magma storage depths can be inferred from geophysical and geochemical observations at the Earth's surface, including ground deformation [*Amelung et al.*, 2000; *Biggs et al.*, 2009; *Hooper et al.*, 2004; *Ofeigsson et al.*, 2011], seismic activity [*Aspinall et al.*, 1998; *Davidge et al.*, 2017; *Gudmundsson et al.*, 1994], and gas emissions [*Burton et al.*, 2007; *McCormick Kilbride et al.*, 2016]. Following eruptions, storage depth estimates can be obtained from petrological analyses of erupted material, through the application of experimentally-calibrated geobarometers [*Putirka*, 2008; *Ridolfi et al.*, 2010; *Yang et al.*, 1996]. Geophysical and petrological constraints are not often combined to study the architecture of sub-volcanic systems, largely because both datasets are seldom simultaneously available for the same eruptions [*Jay et al.*, 2014]. In the rare circumstance where both robust geophysical datasets and rock samples are available, integration can provide better constraints on magma storage depths, additional information about the structure and dynamics of magma plumbing systems, and an improved understanding of the processes responsible for pre-eruptive monitoring signals [*Gudmundsson et al.*, 2016; *Halldórsson et al.*, 2018; *Hartley et al.*, 2018; *Jay et al.*, 2014; *Klügel et al.*, 2015; *Laeger et al.*, 2017; *Longpré et al.*, 2014; *Magee et al.*, 2018; *Stock et al.*, 2018].

The Galápagos Archipelago is one of the most volcanically active regions on Earth, with eruptions typically occurring every 2 years on average, and therefore provides a natural laboratory for volcanology and other Earth sciences [e.g. *Harpp et al.*, 2014]. The most recent eruption of Wolf volcano, located in the north of Isabela Island (Fig. 1), occurred between 25 May – 11 July 2015 and produced ~$116 \cdot 10^6$ m^3 of basaltic lava (*Bernard et al*., 2018), making it one of the most voluminous eruptions in the Galápagos Islands in recent years. Interferometric Synthetic Aperture Radar (InSAR) surface displacement measurements have recorded ground motion at Wolf since 1992 [Fig. 1a; *Bagnardi*, 2014], providing the means to track magma accumulation beneath the surface over more than two decades prior to the 2015 eruption. InSAR data also well image surface displacements caused by dike intrusion and magma withdrawal during the eruption, offering an excellent opportunity to integrate petrological and geophysical techniques to obtain a comprehensive picture of the magmatic plumbing system at an active ocean island volcano. Petrological data from the 2015 eruption allow detailed examination of previously incompletely studied crystallisation conditions and crustal magma processing in the Galápagos Archipelago.

In this study, we present new geodetic models constrained by inversions of InSAR data at Wolf volcano that accurately constrain the depths of pre- and syn-eruptive sources of deformation interpreted as potential areas of magma storage. We then undertake geochemical analysis of erupted material and apply recently developed petrological barometers to establish the pressures of crystallisation, mush entrainment, and magma storage and equilibration in the sub-volcanic system. We show that comparing geophysical constraints with independent petrological barometers can provide mutual verification of results and additional detail about the dynamics and architecture of sub-volcanic systems. This represents the most detailed study of magma storage depths in the Galápagos Archipelago to date and the first attempt to quantitatively reconcile geochemical and geophysical results. Our results are widely applicable to interpreting sub-volcanic processes in the active western Galápagos Archipelago where previous geodetic studies have detected similar patterns of deformation [e.g. *Bagnardi and Amelung*, 2012], and may be important for informing future volcano monitoring. Furthermore, by robustly applying petrological and geophysical methods, accounting for the uncertainties in both datasets, we highlight the utility of multidisciplinary approaches to studying the structure of sub-volcanic systems globally.

2. Geological Background

The western sub-province of the Galápagos Archipelago comprises seven distinct volcanic centres on the islands of Isabela and Fernandina (Fig. 1). These are proximal to the upwelling Galápagos plume and are characterised by frequent eruptive activity relative to the older volcanoes in the eastern archipelago [*Geist et al.*, 2014; *Harpp and Geist*, 2018; *Villagómez et al.*, 2014]. The western

Galápagos volcanoes likely emerged <500 kyr ago [*Kurz and Geist*, 1999] and the erupted products are dominantly basaltic lava and near-vent tephra [*Geist et al.*, 2014].

Wolf is the highest volcano in Galápagos, reaching 1710 m above sea level, and has an 'inverted-soup bowl' morphology, typical of the western sub-province shields [*McBirney and Williams*, 1969]. The volcano is topped by a well-developed caldera (6 km diameter, 700 m deep), which formed through multiple collapse events [*Munro and Rowland*, 1996]. It sits on the north-western extremity of the Galápagos Platform on top of ~11 km thick, ~10 Myr old oceanic crust [*Feighner and Richards*, 1994; *Wilson and Hey*, 1995]. There have been 12 reported basaltic lava eruptions at Wolf volcano in the past 220 years [eight in the last century; *Siebert et al.*, 2011], which occurred either from circumferential fissures on the caldera rim or radial fissures on the flanks [*Chadwick and Howard*, 1991]. Before 2015, the most recent eruption was in 1982, which produced lavas from a vent within the caldera and a secondary fissure on the southeast flank [*Geist et al.*, 2005]. Past Wolf eruptions sampled melts that are enriched in incompatible trace elements, similar to other western Galápagos volcanoes, but show a long-term isotopic depletion in their mantle source, analogous to mid-ocean ridge basalt [MORB; *Geist et al.*, 2005]. The erupted melts have remarkably homogeneous MgO concentrations (typically 5.5–6.5 wt%), interpreted as evidence for thermal and compositional buffering of the magmatic system [maintained at ~1150 +/− 11 °C; *Geist et al.*, 2005]. In contrast, the Al_2O_3 concentrations of pre-2015 lavas (i.e. whole-rock samples) vary significantly, due to plagioclase accumulation from the erosion of a sub-volcanic mush zone [*Geist et al.*, 2005].

2.1. Previous constraints on Galápagos magma storage depths

Due to their remoteness, our knowledge of magma storage depths beneath Galápagos volcanoes is largely based on remote sensing data (almost exclusively space-geodetic data), with limited petrological constraints. On long timescales, most volcanoes in the western archipelago show protracted ground uplift, related to shallow magma accumulation in flat-topped reservoirs at 1–2 km depth beneath the surface [*Amelung et al.*, 2000; *Bagnardi and Amelung*, 2012; *Bagnardi et al.*, 2013; *Chadwick et al.*, 2011; *Xu et al.*, 2016; *Yun et al.*, 2006]. Long-term subsidence, possibly related to crystallisation and contraction of a shallow magma body at ~3 km depth, has also been observed at Alcedo [*Hooper et al.*, 2007]. Evidence for additional, deeper magma storage at >5 km has been identified in InSAR data from Fernandina [*Bagnardi and Amelung*, 2012; *Bagnardi et al.*, 2013; *Chadwick et al.*, 2011], Cerro Azul [*Bagnardi and Hooper*, 2018] and Wolf volcano [*Xu et al.*, 2016], and by seismicity patterns at Sierra Negra [*Davidge et al.*, 2017]. There are currently no geodetic constraints on magma storage depths beneath volcanoes in the eastern Galápagos Archipelago, due to the infrequency of historic eruptions [*Siebert et al.*, 2011] and the apparent absence of clear inter-eruptive deformation.

Current petrological constraints on Galápagos magma storage depths rely entirely on comparison of whole-rock lava compositions with the parameterisation of the MORB olivine + plagioclase + augite + melt (OPAM) pseudo-invariant point defined by *Grove et al.* [1992]. These comparisons were made by eye and, in the western archipelago, individual eruptions return a wide range of magma storage pressures between 1 bar and 3 kbar [i.e. 0–11 km depth; *Geist et al.*, 1998; *Naumann et al.*, 2002]. Together with geophysical constraints and other petrological observations, these barometric estimates have been used to construct a general model of the magmatic systems, in which western Galápagos volcanoes are underlain by vertically extensive mush columns, capped by shallow liquid-rich magma reservoirs [Cerro Azul is an exception as there is no evidence for shallow magma storage; *Geist et al.*, 2014]. The amount of magma processing at different crustal levels and the extent of mixing between magma batches from different storage regions remain unconstrained [*Geist et al.*, 2014]. In contrast with the western Galápagos volcanoes, petrological analyses from the eastern archipelago return storage pressures >5 kbar [*Geist et al.*, 1998]. This is interpreted as indicating a different style of sub-volcanic architecture, in which magmas are stored almost exclusively in the mid-to-lower crust [*Harpp and Geist*, 2018].

3. The 2015 Wolf eruption

After 33 years of quiescence, Wolf volcano began erupting on the 25 May 2015 from an ~800 m long circumferential fissure on the southeast side of the caldera (Fig. 1c). Eyewitnesses on the west flank of the volcano report the onset of eruption between 00.30 and 00.45 (local time) on 25 May, when they felt seismicity and observed an ash plume, illuminated by lava incandescence and volcanic lightning (David Anchundia [an eyewitness to the eruption], personal communication). The eruption was accompanied by a series of seismic events, recorded by an Instituto Geofisico seismometer on Fernandina (FER1), beginning at 23:50 on 24 May and culminating with the largest event (M3.8) at 00:58 on 25 May (www.igepn.edu.ec/servicios/noticias/1007-informe-especial-galapagos-no-2-2015). The first direct observation of erupted lava flows was by the crew of the *La Pinta* tourist ship at 01:29. During this initial phase, the NASA Ozone Monitoring Instrument recorded a major plume extending northwest from the vent and a subsidiary plume extending eastwards; this transported cryptotephra that was detected >1000 km away in Quito [*Bernard et al.*, 2015].

The first lavas produced in the 2015 eruption flowed down the flanks of the volcano and were associated with a >100 m high lava fountain from the southeast summit fissure. Lava initially moved southeast, reaching ~9 km from the vent. After 1–2 days the southeast flow stopped, and activity transitioned to the east flank of the volcano (Fig. 1c). The eastern lava flow reached the sea (~7 km from the vent) between 26–27 May and the circumferential fissure stopped erupting on 2 June. After a hiatus, the eruption briefly resumed from the circumferential fissure on 11 June, before switching to a vent within the caldera on the southeast side on 13 June, producing flows that covered much of the caldera floor (Fig. 1c). The eruption ended on 11 July. In total, $\sim 63 \cdot 10^6$ m^3 of lava were emplaced during the circumferential fissure phase of the eruption (i.e. flows on the volcano flanks), with a further $\sim 53 \cdot 10^6$ m^3 erupted during the subsequent caldera-fill phase (*Bernard et al.*, 2018). The detailed chronology and phenomenology of the eruption is the subject of an ongoing investigation.

Multi-platform surface deformation measurements from InSAR data acquired in the years prior to the 2015 eruption show a ~0.6 m net intra-caldera inflationary signal between 1992 and 2009 and no deformation between 2009 and late-2010 [Fig. 1a; *Bagnardi*, 2014], when routine InSAR data coverage ceased. Poor temporal sampling during 1992–2000 does not allow time-integrated studies of the deformation during this period but data acquired after 2000 have shown near continuous uplift at a rate of ~0.045 cm/yr until the end of 2008. Routine InSAR coverage resumed in December 2014 with the launch of the European Space Agency's Sentinel-1 satellite mission, and co-eruptive surface displacements present a complex pattern that has been interpreted as the superposition of deformation caused by the intrusion of two subvertical dikes feeding the eruptive fissures and the deflationary signal produced by magma withdrawal from two sources, located at ~1 and ~5 km depth, respectively [*Xu et al.*, 2016]. The shallow deflationary source correlates with the depth of pre-eruptive inflation between 1992–1997 [Fig. 1a; *Amelung et al.*, 2000] and 2004–2008 [*De Novellis et al.*, 2017]. The constraints on the deeper source placed by *Xu et al.* [2016] may be affected by the use of an incomplete dataset that does not appropriately include displacements in the far field, south of the volcanic edifice. Far-field deformation measurements are, in fact, diagnostic of source depth. We therefore reanalyse pre- and syn-eruptive surface deformation data with the aim of placing robust constraints on the depths of both magma storage regions and estimate the associated uncertainties using a congruent approach.

4. Data, samples and methods

4.1. InSAR data and geodetic modelling

To estimate source parameters for the shallower deformation source, we use synthetic aperture radar (SAR) data acquired during the long-term pre-eruptive inflationary period by the European Space Agency's (ESA) ENVISAT satellite (Fig. 2). The use of pre-eruptive data allows us to avoid a complicated signal deconvolution otherwise needed for the syn-eruptive data [*Xu et al.*, 2016]. We process 45 SAR images from an ascending track (T061) and 44 images from a descending (T140) track, acquired between January 2004 and December 2008 with a minimum repeat pass of 35 days. The SAR data are used to form interferograms with short temporal and perpendicular baselines to maximise coherence and minimise topographic errors. For each track we apply a chain stacking approach [e.g. *Biggs et al.*, 2007], where we sum the unwrapped interferometric phase of temporally consecutive interferograms to generate cumulative surface displacements maps spanning the five-year interval (Fig. 2a,d). In this approach, the second image used to form each interferogram (commonly referred to as slave image) is the reference image (commonly referred to as master image) used to form the following interferogram, such that orbital and atmospheric contributions from images in the middle of the chain cancel out, and only those relative to the first master and last slave remain.

To estimate source parameters for the deeper source, we use SAR data acquired by ESA's Sentinel-1 satellite and spanning the 2015 eruption (Fig. 3). Large-scale surface displacements caused by pressure changes in a deeper magma reservoir are, in fact, only observed during this eruption. Sentinel-1 syn-eruptive data are only available for the descending pass of the satellite (track T128) and are acquired in the Terrain Observation by Progressive Scans (TOPS) mode. We form three Sentinel-1 independent interferograms (i.e. using different image pairs), one during the circumferential fissure eruptive phase (18 May 2015 – 30 May 2015; Fig. 3a), one spanning the caldera-fill eruptive phase (11 June 2015 – 23 June 2015; Fig. 3d), and a third one measuring the displacements associated with both phases (6 May 2015 – 5 July 2015; Fig 3g). Given the complex deformation pattern within and around the summit caldera caused by the convoluted effect of the opening of the subvertical feeder dikes and shallow source deflation [*De Novellis et al.*, 2017; *Xu et al.*, 2016], we mask out a sub-circular area around the caldera and only use far field data [e.g. *Bagnardi and Amelung*, 2012]. The extent of the mask is constrained using source parameters for the shallower source and the feeder dikes estimated by *Xu et al.* [2016]. We observe that these sources produce line-of-sight displacements that are <0.01 m at radial distances >6 km from the centre of the caldera (grey ellipses in Figure 3).

All interferograms are formed using the InSAR Scientific Computing Environment (ISCE) software [*Rosen et al.*, 2015] and by applying conventional differential InSAR processing techniques for stripmap (Envisat) and TOPS (Sentinel-1) data. Topographic contributions to the interferometric phase are removed using the NASA Shuttle Radar Topography Mission 30-m resolution digital elevation model [*Farr et al.*, 2007], and interferograms are phase-unwrapped using the Snaphu unwrappper [*Chen and Zebker*, 2000] implemented in ISCE. A list of SAR acquisitions, interferograms, and radar look vector information, are provided in the Supporting Information.

Deformation source parameters and uncertainties are estimated using a Bayesian approach implemented in the Geodetic Bayesian Inversion Software [GBIS; *Bagnardi and Hooper*, 2018]. The inversion algorithm samples posterior probability density functions (PDFs) of source parameters using a Markov chain Monte Carlo method, incorporating the Metropolis-Hastings algorithm, with automatic step size selection. Posterior PDFs are calculated considering errors in the InSAR data, which we directly quantify using experimental semivariograms to which we fit an unbounded exponential one-dimensional function with a nugget [*Bagnardi and Hooper*, 2018]. The exponential function is then used to populate the data variance-covariance matrix.

We jointly invert the cumulative displacement maps from the Envisat contemporary pre-eruptive data and estimate source parameters for the shallower source, which we model as a horizontal rectangular dislocation with uniform opening [*Okada*, 1985]. For the Sentinel-1 data, we independently invert each syn-eruptive masked interferogram spanning the different phases of the eruption and infer source parameters for the deeper source, which we model as a finite spherical pressure source with fixed radius r = 1000 m [*McTigue*, 1987]. Other source types with more complex geometries were tested but did not provide statistically significant improvements in reproducing the observed surface displacements. We therefore opted for the source geometry with the lowest number of parameters. Since the elevation range spanned by the InSAR measurements is in all cases <1000 m and the average height of data points is 310 m above sea level, we do not consider the effect of topography when estimating surface displacements. Prior to inversions, all InSAR datasets are subsampled using an adaptive quadtree sampling [*Decriem et al.*, 2010] to reduce the computational burden when calculating the inverse of the data variance-covariance matrix and in forward model calculations. Quadtree is an efficient gradient-based subsampling method that maintains a higher density of data points in areas characterised by higher displacement gradients and vice versa. The algorithm recursively divides a dataset into sets of four polygons until the phase variance of the points within a polygon is below a given threshold. For all models, we assume that the deformation sources are embedded in an isotropic elastic half-space with Poisson's ratio ν = 0.25. Since no detailed prior information on the deformation source parameters are available, prior probability distributions are assumed to be uniform between geologically realistic bounds. In each inversion, posterior PDFs are sampled through 10^6 iterations. Depth estimates are referred to as distance from the surface.

4.2. Petrological samples and methods

Petrological samples were collected from the east flank of Wolf volcano during fieldwork in June 2017 (Fig. 1b). All material was unaltered and collected from low-vesicularity flow interiors where possible. The six lava samples selected for this study are from different flow lobes that formed during 2015 and cover the entire timespan of the initial circumferential fissure phase of the eruption. Intra-caldera lavas were inaccessible. Tephra samples were also collected from seven locations on the east coast of the volcano. No tephra was found on top of any lava flows that formed in 2015, including the initial southeast flow lobe, and we therefore infer that it was expelled during the high lava fountaining episode at the onset of eruption [*Bernard et al.*, 2015].

Lava samples were prepared for microanalysis as polished thin sections. Scoria samples were crushed, and heavy liquid and magnetic separation techniques were used to separate pyroxene crystals from the 40–500 μm size fraction. Crystals and glass fragments were mounted in epoxy, ground and polished for analysis. Samples were examined by back-scattered electron (BSE) imaging to characterise pyroxene zoning patterns and assess glass fragments for the presence of microlites using an FEI Quanta 650F scanning electron microscope (SEM) in the Department of Earth Sciences, University of Cambridge, operating with a 15 kV beam and spot size 4.5–5.

Crystal and glass major and trace elements were analysed using a Cameca SX100 electron microprobe in the Department of Earth Sciences, University of Cambridge. Clinopyroxene was analysed using a 15 kV, 20 nA, defocussed (5 μm) beam. Glass measurements were made using a 15kV, 6 nA, defocussed (10 μm) beam for most elements, with alkalis and SiO_2 analysed first to minimise the effects of electron beam-induced sample damage. SO_2, Cr_2O_3 and MnO were measured in a second glass analysis at 10 nA but Cr_2O_3 was consistently below detection limits. Typical peak counting times were 10–30 s for major elements and 30–90 s for minor elements. Pyroxene crystals were analysed in different textural associations (i.e. phenocrysts, glomerocrysts, tephra crystals) by point analysis or line transects, to characterise the zoning textures identified by SEM. Relative 2σ precision was estimated from repeat analyses of secondary standards and is typically better than ±5% for most elements, except Cr_2O_3 (±8.8%) and MnO (±34.1%) in clinopyroxene and SO_2 (±11.1%), K_2O (±17.4%), P_2O_5 (±17.8%) and MnO (±43.9%) in glass. To ensure consistency between analytical sessions, glass compositions were normalised using VG-2 as an internal standard [*Jarosewich et al.*, 1980]. All pyroxene formula recalculations are on a six-oxygen (6O) basis and phase components are defined according to *Putirka* [2008].

4.3. Thermobarometric modelling

The OPAM barometer assesses the pressure-dependent position of the olivine–plagioclase–augite–melt pseudo-invariant point [*Grove et al.*, 1992], thus quantifying the pressure of magma equilibration. This was initially parameterised as a function of the melt X_{Al}, X_{Ca} and X_{Mg} (where X is mole fraction) over a range of temperatures and melt major compositions by *Yang et al.* [1996]. We apply a recent reparameterization by *Voigt et al.* [2017], which accounts for the effects of oxygen fugacity (fO_2) and melt Cr contents on the OPAM point location. Our calculations assume negligible melt Cr (based on our EPMA data) and FeO/FeO* = 0.85 (where FeO* is total FeO + Fe_2O_3), which approximates an fO_2 close to the fayalite-magnetite-quartz buffer, similar to that measured by *Peterson et al.* [2015] in Galápagos lavas. A prerequisite of the OPAM approach is that liquids are multiply-saturated in olivine, plagioclase and clinopyroxene. Although visual assessment of 2015 Wolf lavas suggests that these melts were multiply-saturated (i.e. all phases present, euhedral crystal forms, no resorption of crystal rims), this appraisal is qualitative and is not possible in low-crystallinity tephra where crystals were extracted by density and magnetic separation (i.e. preserve no textural information). We therefore filter our input liquid compositions for multiple saturation using the approach of *Hartley et al.* [2018]. This calculates a probability factor for three-phase saturation (P_F), with the OPAM model returning reliable pressures at P_F >0.8. Although this filter falsely rejects a minority of multiply-saturated liquids, it minimises the OPAM uncertainty [*Hartley et al.*, 2018]. The standard error of estimate (SEE) has not been quantified for the *Voigt et al.* [2017]

parameterisation and we therefore assume a conservative SEE equal to that of the original *Yang et al.* [1996] model (±1.4 kbar).

Clinopyroxene-melt thermobarometry estimates crystallisation conditions through pressure-sensitive jadeite component reactions [*Putirka*, 2008]. *Putirka et al.* [1996] developed the first barometric model relating clinopyroxene-melt equilibria to crystallisation pressures in basaltic systems and we utilise the most recent reparameterization with the lowest SEE [±1.4 kbar; *Neave and Putirka*, 2017]. Following *Neave and Putirka* [2017], we solve the barometric equations iteratively with the thermometric equation 33 of *Putirka* [2008; SEE ±28 °C]. Our calculations assume an anhydrous melt with FeO/FeO* = 0.85 [*Peterson et al.*, 2015], consistent with our OPAM modelling. Robust application of clinopyroxene-melt thermobarometers requires identifying liquid compositions in equilibrium with analysed pyroxenes. To avoid biasing our results and to maximise the number of equilibrium clinopyroxene-melt pairs for barometry, we make no prior assumptions about the nature of liquids in equilibrium with our pyroxene crystals. Instead, we implement a melt-matching algorithm [as in *Neave and Putirka*, 2017; *Winpenny and Maclennan*, 2011], testing each of our pyroxene analyses against our tephra glass analyses and the whole-rock and submarine glass compositions of pre-2015 Wolf lavas measured by *Geist et al.* [2005]. Crystals with strong sector zoning are excluded after visual assessment [*Neave and Putirka*, 2017] and equilibrium liquids are identified where K_D(Fe-Mg) is within ±0.03 of that predicted from a pyroxene analysis and diopside-hedenbergite (DiHd), enstatite-ferrosillite (EnFs) and calcium Tschermak's (CaTs) components are within 1 SEE [*Mollo et al.*, 2013; *Putirka*, 1999; *Putirka*, 2008]. Where pyroxene analyses match with multiple input liquids within uncertainty of the equilibrium tests, we report mean pressure and temperature conditions estimated from all potential equilibrium liquids.

Data are evaluated using kernel density estimates (KDEs), which give a non-parametric probability density function of a random variable, analogous to a smoothed frequency histogram but with a greater statistical significance [*Rudge*, 2008; *Thomson and Maclennan*, 2012]. The shape of a KDE curve strongly depends on the chosen bandwidth. To ensure that KDEs have physical meaning (i.e. all peaks are significant and no real peaks are smoothed out in data processing), we calculate the bandwidth with the method of *Sheather and Jones* [1991]. Although crustal density is not well constrained in Galápagos, the crustal velocity profile and Moho depth beneath Wolf are comparable to Hawaii [*Hill and Zucca*, 1987; *Villagómez et al.*, 2011]. Hence, we convert pressures to depths using the polynomial Hawaiian depth vs pressure curve of *Putirka* [1997] and all depths are measured relative to the surface (i.e. the caldera floor).

5. Results

5.1. Geodetic modelling results

The inversion of Envisat pre-eruptive InSAR data recording intra-caldera inflation confirms that it is best explained by opening of a ~1.8 x 2.3 km flat-topped source at 1.1 km depth (posterior PDFs for all parameters are shown in Supporting Fig. S1). A comparison between the observed displacements and those predicted using the maximum *a posteriori* probability solution is shown in Figure 2.

In the case of the deeper source, inversions of the three Sentinel-1 syn-eruptive datasets provide source centroid depth estimates ranging between 6.1–8.8 km beneath the surface (posterior PDFs for all parameters are shown in Supporting Figs S2–S4). In detail, estimates based on InSAR data spanning the circumferential fissure phase of the eruption locate the source at 6.5–7.9 km, those for the caldera-fill phase at 6.1–7.5 km, and those for the entire event at 6.7–8.8 km depth (depth ranges express the 2.5 and 97.5 percentiles of posterior PDFs). Sources with maximum posteriori probability solutions are centred at 7 km, 6.7 km, and 7.6 km depth, respectively, and comparisons between the observed displacements and those predicted using the maximum posteriori probability solutions are shown in Figures 3b, 3e, and 3h. Our results estimate that this source is ~2 km deeper than inferred by *Xu et al.* [2016] who, in some cases, used the same InSAR data. This discrepancy is likely due to our use of far field data, which was excluded in the study of *Xu et al.* [2016].

5.2. Petrological results

5.2.1. Sample petrography

Lavas from the 2015 eruption are composed of vesicular porphyritic basalt. The groundmass is microcrystalline and contains acicular plagioclase laths, with anhedral olivine, clinopyroxene and ilmenite, and minor interstitial glass. Macrocrysts include euhedral plagioclase (<4 mm, ~5 vol.%) and euhedral or subhedral clinopyroxene (<1 mm, ~2 vol.%) and olivine (<1 mm, <1 vol.%). These occur in two principal textural associations: (1) isolated phenocrysts surrounded by groundmass and (2) gabbroic glomerocrystic aggregates containing two or more touching or intergrown crystals of plagioclase + clinopyroxene +/− olivine, with minor microcrystalline interstitial groundmass. Many plagioclase macrocrysts show evidence of synneusis. Tephra samples are highly vesicular reticulite, dominantly composed of quenched glass with very few microlites. Although the tephra is crystal poor, macrocrysts separated from the 40–500 μm size fraction include plagioclase, clinopyroxene and olivine (in decreasing modal abundance). No textural information is available from these crystal separates (i.e. it is not possible to distinguish between potential phenocrysts or glomerocrysts).

Clinopyroxene zoning textures were studied to ensure thorough compositional characterisation of the crystal cargo from the 2015 eruption. Most crystals in lava samples show concentric oscillatory zoning, which is weak in phenocrysts but occasionally more strongly defined in glomerocrysts, with small internal resorption horizons. A minority of glomerocryst clinopyroxenes also include well-defined cores, which are dark in back-scattered electron (BSE) images. These cores are not resorbed and are overgrown by oscillatory zoned mantles (Fig. 4a). Some phenocrystic and glomerocrystic pyroxenes additionally show minor sector zoning, with oscillatory zones cross-cutting sector boundaries. Only a very small number of crystals have strongly defined sector zones (Fig. 4b). Clinopyroxenes in both textural associations typically have a thin, well-defined rim zone, which is intergrown with groundmass microlites. This rim is concentric in phenocrysts but only occurs on crystal faces in contact with the groundmass in glomerocrysts (Fig. 4a,b). Our interpretation is that these rims grew within the lava flows at the surface. Clinopyroxene crystals in tephra samples are typically unzoned or have weak oscillatory zoning, like those in lava samples. A small number of tephra crystals are texturally distinct in BSE images, with zoning patterns that are absent in lava samples. These include clinopyroxenes with faint patchy zoning, a single analysed crystal with a concentric bright rim around an unzoned core (Fig. 4c), and rare crystals with highly resorbed bright cores, mantled by a concentric darker rim (Fig. 4d). The pyroxenes with highly resorbed cores contain abundant mineral and melt inclusions. Thin rim zones, analogous to those inferred to have grown at the surface in lava samples (Fig. 4c), are absent in crystals from tephra samples.

5.2.2. Melt and pyroxene compositions

Excluding Al_2O_3-enriched lavas that have accumulated feldspar, whole-rock analyses from pre-2015 Wolf lavas plot with decreasing Al_2O_3 and CaO/Al_2O_3 and increasing incompatible element concentrations (e.g. K_2O, TiO_2) with decreasing MgO, consistent with olivine, plagioclase and clinopyroxene crystallisation [Fig. 5; *Geist et al.*, 2005]. Our 2015 tephra glass analyses and submarine glass analyses from pre-2015 lavas [*Geist et al.*, 2005] plot on the same compositional array. The tephra glasses have a narrow compositional range with 5.12–6.25 wt% MgO but are slightly heterogeneous outside of analytical uncertainty for most major elements (Supporting Table S1). They have intermediate compositions on the whole-rock array: most bulk lavas have more primitive compositions (higher MgO, lower incompatible elements) than the tephra glasses but a small number extend to more evolved compositions (Fig. 5). Pre-2015 submarine glasses are also more compositionally diverse than the 2015 tephra glass, extending to both more primitive and evolved compositions.

Clinopyroxene crystals in lava samples are diopsidic ($Di_{>96}$), with $En_{40–49}Fs_{9–16}Wo_{39–46}$ (Supporting Table S2). They plot on a well-defined compositional trend, with a strong negative correlation between X_{Mg} and X_{Ti}, X_{Al} and X_{Na} (Fig. 6). Although there is overlap between populations, KDEs highlight a compositional distinction between pyroxene crystals in different textural associations (Fig. 6a): glomerocrysts typically have high X_{Mg} (~0.86–0.88 on a 6O basis) and X_{Cr} (<0.026) relative to phenocrysts (X_{Mg} ~0.79, X_{Cr} <0.0089). All analyses from crystals with strong sector zoning (e.g. Fig. 4b) diverge from the compositional trend towards high X_{Mg} and low X_{Ca} (Fig. 6), likely due to disequilibrium crystallisation at high growth rates [*Mollo et al.*, 2010]. Clinopyroxene crystals from tephra samples are also diopside-rich ($Di_{>95}$) but exhibit greater diversity in their enstatite and ferrosillite components than crystals from the lava ($En_{19-47}Fs_{9-38}Wo_{35-46}$; Supporting Table S2). Most crystals from tephra samples plot on the same compositional trend as crystals from lava samples, with an X_{Mg} KDE peak at 0.85 (Fig. 6a), high X_{Cr} and low X_{Ti} and X_{Al}. In general, these crystals are compositionally analogous to the glomerocrysts in lava samples, with only a small number correlating with the main phenocryst population. The tephra samples also contain a sub-set of clinopyroxene crystals that are compositionally distinct from those in lava samples, extending to very low X_{Mg} values (0.36–0.68) and very high X_{Fe*}. These crystals contain negligible X_{Cr} and are poor in X_{Al} and X_{Ca} relative to crystals on the main compositional trend (Fig. 6).

Oscillatory zoning textures observed in BSE images correspond with small fluctuations in the clinopyroxene major components (En, Fs, Wo). In lava crystals with defined core-mantle zonation (e.g. Fig. 4a), the cores are relatively SiO_2 and MgO enriched and FeO*, CaO TiO_2, Al_2O_3 and Cr_2O_3 depleted, with higher a Mg# [$X_{Mg}/(X_{Mg}+X_{Fe*})$] than the mantles. These cores are compositionally distinct from crystals with strong sector zoning, suggesting that they are not sectioning artefacts where sector zoned crystals are cut perpendicular to the *c*-axis [*Welsch et al.*, 2016]. In the tephra crystal with a defined rim zone, the core plots on the main clinopyroxene compositional trend but the rim is Mg poor with a markedly lower Mg# (Fig. 4c). The lowest measured pyroxene X_{Mg} compositions (and highest X_{Fe*}) are in the crystals from tephra samples that have heavily resorbed cores or clear patchy zoning textures. In the former, the heavily resorbed crystal cores have very low Mg# and are overgrown by higher Mg# mantles (Fig. 4d).

5.2.3. Thermobarometric modelling results

We applied the OPAM barometer [*Voigt et al.*, 2017] to 58 tephra glass analyses from the 2015 Wolf eruption. The statistical test for three-phase saturation returned acceptable results ($P_F > 0.8$) for ~60% of the input analyses. These high P_F liquids have a restricted range of MgO contents between 5.55–6.06 wt% and do not include either the most MgO rich or poor glass analyses (Fig. 7a). This does not preclude that these more primitive or evolved liquids were ternary saturated, as the statistical test can return false negatives [*Hartley et al.*, 2018]. However, the results with $P_F < 0.8$ are excluded to ensure the reliability of barometric results. The mean pressure of magma equilibration obtained using the

OPAM method is 2.8 ±0.7 kbar (1σ of calculated pressures). There is no correlation between OPAM pressures and any glass compositional parameter outside of model uncertainty and there is only a single peak in the probability distribution of OPAM pressure estimates (Fig. 7b).

To identify equilibrium pairs for clinopyroxene-melt barometry, we tested 52 phenocryst and 280 glomerocryst clinopyroxene analyses from lava samples and 170 clinopyroxene analyses from tephra samples against our tephra glass analyses from the 2015 eruption and the pre-2015 whole-rock and submarine glass analyses from Wolf volcano measured by *Geist et al.* [2005]. Matches were found for 35 phenocryst, 162 glomerocryst and 73 tephra crystal analyses (Fig. 6). The equilibrium tests did not match any pyroxene analyses with Al_2O_3-enriched whole-rock analyses that include accumulated plagioclase and do not represent liquids (Fig. 5). In general, the most Mg-rich clinopyroxene analyses return equilibrium matches with the most primitive (high-MgO) liquids. Hence, lava glomerocrysts and crystals from tephra samples typically return equilibrium matches with liquids similar to more primitive whole-rock and submarine glass compositions and phenocrysts from lava samples typically match with liquids similar to evolved whole-rock, submarine glass or tephra glass analyses (Fig. 5a). In detail, pyroxene analyses often return equilibrium matches with both whole-rock and glass analyses, but we seek to avoid making *a priori* assumptions about the nature of equilibrium clinopyroxene-liquid pairs and hence average all potential liquids that match each pyroxene analysis; using glass or whole-rock compositions individually makes negligible difference to the barometric results. Equilibrium matches with our input liquids were almost exclusively restricted to pyroxene analyses that plot on the main compositional trend; very few equilibrium liquids were identified for the sub-set of crystals from tephra samples with low X_{Mg} contents and those that did return equilibrium matches are only slightly X_{Mg}-depleted relative to the main population at equivalent X_{Al} (Fig. 6).

In lava samples, clinopyroxene crystals in glomerocrysts return a mean clinopyroxene-melt crystallisation pressure of 2.8 ±0.6 kbar (1σ of calculated pressures). The probability distribution is not perfectly Gaussian, as a small number of analyses at the rims of glomerocrysts return markedly low pressures (~1 kbar). However, the mean pressure correlates with the major peak in the KDE (Fig.

8a). Thermometric modelling of these pyroxenes gives an average crystallisation temperature of 1164 ±11 °C (1σ of calculated temperatures), with an irregular probability distribution, peaking at 1160 °C and 1173 °C (Fig. 8b). Clinopyroxene phenocrysts return a mean crystallisation pressure of 3.2 ±0.7 kbar (peak at 3.3 kbar) and a lower average crystallisation temperature of 1151 ±9 °C, both with approximately normally distributed KDEs (Fig. 8). Clinopyroxene-melt barometric results for crystals from tephra samples have more complex probability functions than those from lava samples: they record average crystallisation pressures of 2.9 ±0.8 kbar but the probability distribution is skewed, with a peak at 3.1 kbar and a long tail towards lower pressures (Fig. 8a). Thermometric modelling of pyroxene crystals from tephra samples returns a similarly skewed distribution with an average crystallisation temperature of 1164 ±15 °C, the largest peak at 1170 °C, and a pronounced tail towards lower temperatures (Fig. 8b). Analyses that return the lowest pressure estimates for a given crystal are not necessarily at the rim, but the estimated pressures are within model uncertainty (SEE = ±1.4 kbar) of those calculated for points closer to the crystal exteriors. A single negative pressure estimate is within uncertainty of other low-pressure clinopyroxene-melt barometric results.

Crystallisation pressures calculated from clinopyroxene-melt barometry do not show an obvious relationship with either the Mg# of pyroxene analyses (Fig. 8a) or their equilibrium liquids. However, there is a positive correlation between crystallisation temperatures and the Mg# of the pyroxene crystals (Fig. 8b) and their equilibrium liquids. Our most probable crystallisation temperatures agree well with the range of Wolf magma storage temperature estimated from MELTS models by *Geist et al.* [2005]. There is no clear connection between pyroxene zoning textures in lava samples and crystallisation conditions within the uncertainty of our dataset. In crystals from tephra samples, analyses from the core of the crystal with a low Mg# rim (Fig. 4c) return pressures close to the peak in the tephra clinopyroxene-melt barometry probability distribution and points slightly inside of the rim zone plot within the low-pressure tail. Crystallisation pressures could not be calculated for the low Mg# rim of this crystal, any zones within the tephra crystals with highly resorbed cores or the patchy zoned crystals, as they are not in equilibrium with any of our input liquids.

6. Discussion

6.1. Deciphering the Wolf crystal cargo

Glomerocrysts in lavas from the 2015 Wolf eruption are texturally analogous to those in samples from other ocean islands, which are interpreted as fragments of disaggregated sub-volcanic mush [*Holness et al.*, 2007; *Neave et al.*, 2014; *Sliwinski et al.*, 2015; *Stock et al.*, 2012]. Abundant glomerocrysts in the products of other eruptions from the western Galápagos Archipelago [*Chadwick et al.*, 2011; *Cullen et al.*, 1989; *Geist et al.*, 1995; *Sinton et al.*, 1993] attest to sub-volcanic mush zones across the region [*Geist et al.*, 2014]. At Wolf volcano, the presence of a gabbroic mush zone has previously been inferred from whole-rock data [*Geist et al.*, 2005]. Although some phenocrysts in lavas from the 2015 eruption could also have been entrained from this mush, they are typically compositionally and texturally distinct from glomerocrysts, with planar low-index growth faces, consistent with growth in a liquid-rich environment [e.g. Fig. 4b; *Holness et al.*, 2017a]. Plagioclase synneusis further attests to crystallisation under liquid-rich conditions [*Holness et al.*, 2017b].

Excluding samples that show evidence for plagioclase accumulation, glass and whole-rock data from Wolf volcano appear to follow a single liquid line of descent (Fig. 5), which is supported by the majority of clinopyroxene analyses plotting on a single compositional trend (Fig. 6). Although there is significant overlap between the crystal populations, phenocrysts typically have lower X_{Mg} contents (and Mg#; Fig. 6) and calculated crystallisation temperatures (Fig. 8b) than glomerocrysts, and return equilibrium matches with our more evolved input liquids (Fig. 5a). This suggests that the crystal mush formed from a slightly more primitive melt than the phenocrysts that crystallised in a liquid-rich magma body.

Most clinopyroxene analyses from tephra samples plot on the same compositional trend as crystals in the lava samples and are compositionally analogous to the glomerocrysts (Fig. 6); they are in equilibrium with compositionally similar melts (Fig. 5) and have similar crystallisation temperatures (Fig. 8). Although no textural information is available for tephra crystals, this geochemical comparison suggests that most crystals sampled by the early explosive phase are derived from the same sub-volcanic mush zone as the later effusive phase. The sub-set of pyroxene analyses from tephra samples that have low X_{Mg} contents do not plot on the main trend and do not return an equilibrium match with any of the input erupted liquids (Fig. 6) but their low Mg# is consistent with crystallisation from more evolved liquids than those from the main compositional trend. The diversity of zoning textures in these evolved crystals indicates a mixed crystal cargo, with individual grains recording different growth histories. Specifically, the presence of both normal zoning (core-to-rim decrease in Mg#; Fig. 4c) and resorptional reverse zoning (core-to-rim increase in Mg#; Fig. 4d) suggests crystallisation under open-system conditions [*Streck*, 2008; *Ubide and Kamber*, 2018].

6.2. Architecture of the sub-volcanic plumbing system

Our analyses of InSAR data and geodetic modelling results indicate the presence of at least two crustal magma storage regions beneath Wolf volcano, consistent with previous studies [*Xu et al.*, 2016]. We model a shallow, flat-topped magma reservoir at 1.1 km beneath the surface and centred below the summit caldera. This source overlies a second deeper storage region modelled as a pressurised spherical cavity at 6.1–8.8 km. The Wolf caldera floor is located ~1 km above sea level and ~2 km above the top of the northern periphery of the Galápagos Platform bathymetric high, which in turn rises ~2.5 km above the Pacific Ocean floor [*Geist et al.*, 2005]. Hence, the shallow deformation source is likely within the volcanic pile, approximately at sea level (Fig. 9). This is similar to the shallow magma storage regions beneath Fernandina and Sierra Negra volcanoes, which are within the edifices at ~1.1 km (below sea level) and 1.9 km (below the surface), respectively [*Bagnardi and Amelung*, 2012; *Yun et al.*, 2006].

Our OPAM results are broadly distributed, with the most probable carrier liquid equilibration depth at 9.8 ±2.7 km (1σ of calculated depths). Clinopyroxene-melt barometry returns most probable crystallisation depths of 9.9 ±2.2 km and 11.2 ±2.4 km for glomerocrysts and phenocrysts in lava samples, respectively, and 10.1 ±2.8 km for pyroxene crystals in tephra samples. Hence, the crystallisation depths for clinopyroxene crystals in different textural associations overlap within uncertainty and are comparable with magma storage depths derived from OPAM barometry. The crust beneath the Wolf edifice is ~11 km thick [*Feighner and Richards*, 1994] and our petrological barometry therefore reveals that most of the material expelled during the 2015 eruption was sourced from a lower crustal storage region, at or only slightly above the Moho (Fig. 9). The probability distributions for our petrological magma storage depth estimates overlap with the depth of the lower InSAR deformation source (Fig. 9). Erupted volumes and geodetically-estimated volume changes are not directly comparable without accounting for the physical characteristics of a multi-phase magma in the reservoir (e.g. compressibility) and of lava at the surface (e.g. conversion of bulk volume into dense rock equivalent volume). However, our finding that the erupted material is mostly sourced from the lower crust is qualitatively consistent with a significantly greater syn-eruptive volume loss from the deep geodetic source (between $43 \cdot 10^6$ and $64 \cdot 10^6$ m^3 [2.5 and 97.5 percentiles of posterior PDFs]; this study) than the shallow source (~$2.8 \cdot 10^6$ m^3; *Xu et al.,* 2016).

Although the clinopyroxene-melt barometry probability distribution for crystals from tephra samples shows a tail towards low pressures and a few glomerocryst rim analyses return low pressure crystallisation estimates (Fig. 8), there is little petrological evidence of erupted material being sourced from the shallow storage region identified in our geodetic models (Fig. 9). We nevertheless note that tephra samples contain a small number of texturally and compositionally distinct pyroxene crystals that have experienced open-system interaction between evolved and primitive liquids (Fig. 4). These crystals are absent from lava samples and are not in equilibrium with any known magmatic liquids (Fig. 6), inhibiting calculation of their crystallisation pressures. We propose that these evolved crystals were derived from part of the sub-volcanic system that was incorporated into initially ascending melts but not into the magmas feeding later lava flows. This region must have been volumetrically small compared to the ascending magma, so that only a small number of crystals were incorporated into the ascending material, and the melt composition was largely overprinted by mixing during interaction with ascending liquids; magma mixing on short pre-eruptive timescales is supported by the minor heterogeneity in tephra glass compositions (Figs 4, 6). The most likely possibility is that the evolved crystals were sourced from the region of shallow inflation, which underwent periods of cooling and crystallised in the upper crust (e.g. during hiatuses in deformation when no new melt entered system) but unpicking the detailed petrogenesis of these evolved components is beyond the scope of this paper.

6.3. Pre- and syn-eruptive processes

Figure 10 summarises processes before and during the 2015 Wolf eruption, based on our interpretation of geophysical and petrological data. Before the eruption (t_1), the volcano showed shallow inflation as new melts intruded into a shallow sill at 1.1 km depth: inflation occurred between 1992–1997 (poor temporal sampling inhibits determining whether this was persistent or episodic) and was continuous between 2000–2009 [Fig. 1a; *Bagnardi*, 2014]. Cooling and crystallisation, punctuated by periodic recharge events, gave rise to complex pyroxene zoning textures including evolved compositions in shallow parts of the system. There was no deformation between 2009 and late-2010, as no new melts entered the shallow sill (t_2). There is no evidence for renewed deformation before the eruption in 2015 but we cannot exclude it, due to a gap in routine SAR coverage. During the eruption, magma ascended from the lower crust, causing deflation at 6.1–8.8 km depth (maximum probability 7.6 km). The first magma to ascend erupted in a high fountaining episode, forming the reticulitic tephra. This carried a mixed crystal cargo, including mush-derived crystals from the deep storage region (i.e. compositionally analogous to lava glomerocrysts) and crystals with complex zoning that were entrained on ascent, potentially from the upper crustal sill detected by InSAR (t_3). Magmas that ascended later fed lava flows and only carried crystals from the lower crustal storage region, sampling both liquid-rich (phenocrysts) and mushy (glomerocrysts) crystallisation regions (t_4). Our OPAM and clinopyroxene-melt barometry demonstrates that almost all the material expelled during the 2015 eruption was sourced from the lower crust, with very little petrological evidence for material conceivably sourced from the shallow sill. This likely reflects the relative sizes of the two storage regions, with only a small amount of material from the upper–mid crust mixing with a much larger volume of magma ascending from depth.

7. Conclusions and implications for Galápagos magma storage

Previous models of sub-volcanic systems in the western Galápagos Archipelago typically infer vertically protracted magma systems, capped by liquid-rich sills or magma chambers in the upper crust [*Geist et al.*, 1998; *Geist et al.*, 2014]. In contrast, volcanoes in the eastern archipelago are thought to be characterised by magma storage in the mid-to-lower crust [*Harpp and Geist*, 2018]. These interpretations are largely based on geophysical data in the western archipelago, but solely on petrological constraints and geomorphological observations in the east [*Geist et al.*, 2014]. Our integrated petrological and geophysical data from Wolf volcano (in the western archipelago) support at least two discrete zones of magma storage in the sub-volcanic system: a small upper crustal sill at 1.1 km and a lower crustal magma storage zone at >6.1–8.8 km, which contains both mushy and liquid-rich regions (Figs 9, 10). Almost all the material expelled during the 2015 eruption was sourced from the deeper storage region. Hence, our data do not support a fully trans-crustal magmatic system [e.g. *Cashman et al.*, 2017; *Marsh*, 1996] before the 2015 eruption but rather suggest that the majority of magma equilibration, crystallisation and mush entrainment occurred in the lower crust (Fig. 9). This is consistent with observations from other ocean islands, where recent studies have shown that eruptions may be supplied by melts ascending directly from the lower crust or uppermost mantle [*González et al.*, 2015; *Longpré et al.*, 2014; *Maclennan et al.*, 2001; *Winpenny and Maclennan*, 2011]. Although shallow sills in the western archipelago may be relatively small, mixing between shallow and deep melts could nonetheless be responsible for the spread in previous barometric results from the western Galápagos, which are based on whole-rock analyses [*Geist et al.*, 1998].

Patterns of ground deformation similar to those identified before the 2015 Wolf eruption have recently been identified elsewhere in the western Galápagos Archipelago (e.g. at Fernandina and Cerro Azul), with shallow inter-eruptive inflation and significant deflation of a deeper magma storage region during eruptions or major dike intrusion events [*Bagnardi and Amelung*, 2012; *Bagnardi and Hooper*, 2018; *Bagnardi et al.*, 2013; *Geist et al.*, 2008b]. Based on our observations from Wolf volcano, these deep deflationary sources must reflect melt extraction from large lower crustal magma storage regions or mush columns, from which most of the erupted material is sourced. This is supported by earthquake locations and a major low velocity zone imaged by seismic tomography in the lower crust beneath Sierra Negra [*Davidge et al.*, 2017; *Tepp et al.*, 2014]. In this case, significant magma storage and processing in the lower crust may not be restricted to the eastern Galápagos sub-province but could also occur in the western archipelago. Volcanoes in the western sub-province are also underlain by small shallow sills, which we hypothesise may be ephemeral super-solidus features, sustained by high magma supply rates close to the focus of the Galápagos plume [*Villagómez et al.*, 2014] and with further magma ascent inhibited by crustal stresses associated with the summit calderas [*Corbi et al.*, 2015]. *Geist et al.* [2014] suggest that shallow magma may not be maintained in the eastern archipelago because volcanoes are in a dying phase, away from the plume head. In any event, the results presented here show that little crystallisation and differentiation occurs in the upper part of the magmatic plumbing system: most of the compositional variation is imparted in the lower crust.

Although Wolf volcano underwent a prolonged period of magma accumulation in the shallow crust, this did not immediately precede the 2015 eruption and was not where most of the erupted magma was stored. This has broad implications for global volcano monitoring, highlighting a fundamental disconnection between inflation and eruption: long-term shallow inflation does not necessarily represent a precursory signal before eruptions but could instead characterise typical inter-eruptive activity [e.g. *Biggs et al.*, 2014]. In Galápagos, genuine pre-eruptive 'warning' signs may be characterised by seismicity or other signs of magma movement in the lower crust, as identified before the 2005 eruption of Fernandina [*Bagnardi and Amelung*, 2012].

Acknowledgements

MJS was supported by a Charles Darwin and Galápagos Islands Junior Research Fellowship at Christ's College, Cambridge. MB was supported by the NERC Centre for the Observation and Modelling of Earthquakes, Volcanoes and Tectonics (COMET) and by an appointment to the NASA Postdoctoral Program at the Jet Propulsion Laboratory, administered by the Universities Space and Research Administration (USRA) through a contract with NASA. DAN was supported by the Alexander von Humboldt Foundation and the German Research Foundation (NE 2097/1–1). MLMG was supported by a NERC studentship (NE/L002507/1). Additional fieldwork funding was provided by the Jeremy Willson Charitable Trust (administered by the Geological Society of London) and the Mineralogical Society of Great Britain and Ireland. Envisat data were provided by ESA through the GEO Geohazards Supersite (http://supersites.earthobservations.org). Sentinel-1 interferograms were derived from Copernicus SAR data obtained at https://schihub.copernicus.eu and maps in Fig. 1 were created using JAXA ALOS imagery from http://www.eorc.jaxa.jp/. This work would not have been possible without significant support from the Charles Darwin Foundation and the Galápagos National Park. We are grateful to Sally Gibson and Antonio Proaño for their assistance in the field, and Yu Zhou, Tui De Roy and Gabriele Gentile for help with fieldwork planning and logistics. We thank David Anchundia for providing a visual report of the 2015 eruption and Roel van Elsas for mineral separation. The manuscript was greatly improved by constructive reviews from Keith Putirka and an anonymous reviewer. The data for this paper are available in the supporting information.

References

Amelung, F., Jónsson, S., Zebker, H., and Segall, P. (2000). Widespread uplift and 'trapdoor' faulting on Galapagos volcanoes observed with radar interferometry, *Nature*, *407*(6807), 993-996. https://doi.org/10.1038/35039604

Aspinall, W. P., Miller, A. D., Lynch, L. L., Latchman, J. L., Stewart, R. C., White, R. A., and Power, J. A. (1998). Soufrière Hills eruption, Montserrat, 1995–1997: Volcanic earthquake locations and fault plane solutions, *Geophysical Research Letters*, *25*(18), 3397-3400. https://doi.org/10.1029/98GL00858

Bagnardi, M. (2014). *Dynamics of magma supply, storage and migration at basaltic volcanoes: Geophysical studies of the Galápagos and Hawaiian volcanoes*, (PhD thesis). Miami, FL: University of Miami.

Bagnardi, M., and Amelung, F. (2012). Space- geodetic evidence for multiple magma reservoirs and subvolcanic lateral intrusions at Fernandina Volcano, Galápagos Islands, *Journal of Geophysical Research: Solid Earth*, *117*(B10), B10406. https://doi.org/10.1029/2012JB009465

Bagnardi, M., and Hooper, A. (2018). Inversion of surface deformation data for rapid estimates of source parameters and uncertainties: a Bayesian approach, *Geochemistry, Geophysics, Geosystems*, *19*. https://doi.org/10.1029/2018GC007585

Bagnardi, M., Amelung, F., and Poland, M. P. (2013). A new model for the growth of basaltic shields based on deformation of Fernandina volcano, Galápagos Islands, *Earth and Planetary Science Letters*, *377-378*, 358-366. https://doi.org/10.1016/j.epsl.2013.07.016

Bernard, B., Ramón, P., Wright, H., Guevara, A., Hidalgo, S., Pacheco, D. et al. (2015). *Preliminary results on the 2015 eruption of Wolf Volcano, Isabela Island, Galápagos: chronology, dispersion of the volcanic products, and insight into the eruptive dynamics*. Paper presented at AGU Fall Meeting, San Francisco, CA.

Bernard, B., Stock, M. J., Coppola, D., Hidalgo, S., Bagnardi, M., Gibson, S., et al. (2018). Chronology and phenomenology of the 1982 and 2015 Wolf volcano eruptions, Galápagos Archipelago. *OSF*. https://doi.org/10.17605/OSF.IO/93PKR

Biggs, J., Anthony, E. Y., and Ebinger, C. J. (2009). Multiple inflation and deflation events at Kenyan volcanoes, East African Rift, *Geology*, *37*(11), 979-982. https://doi.org/10.1130/G30133A.1

Biggs, J., Wright, T., Lu, Z., and Parsons, B. (2007). Multi-interferogram method for measuring interseismic deformation: Denali Fault, Alaska, *Geophysical Journal International*, *170*(3), 1165-1179. https://doi.org/10.1111/j.1365-246X.2007.03415.x

Biggs, J., Ebmeier, S. K., Aspinall, W. P., Lu, Z., Pritchard, M. E., Sparks, R. S. J., and Mather, T. A. (2014). Global link between deformation and volcanic eruption quantified by satellite imagery, *Nature Communications*, *5*, 3471. https://doi.org/10.1038/ncomms4471

Burton, M., Allard, P., Muré, F., and La Spina, A. (2007). Magmatic gas composition reveals the source depth of slug-driven Strombolian explosive activity, *Science*, *317*(5835), 227-230. https://doi.org/10.1126/science.1141900

Cashman, K. V., Sparks, R. S. J., and Blundy, J. D. (2017). Vertically extensive and unstable magmatic systems: A unified view of igneous processes, *Science*, *355*(6331), eaag3055. https://doi.org/10.1126/science.aag3055

Chadwick, W. W., and Howard, K. A. (1991). The pattern of circumferential and radial eruptive fissures on the volcanoes of Fernandina and Isabela islands, Galapagos, *Bulletin of Volcanology*, *53*(4), 259-275. https://doi.org/10.1007/BF00414523

Chadwick, W. W., Jónsson, S., Geist, D. J., Poland, M., Johnson, D. J., Batt, S. et al. (2011). The May 2005 eruption of Fernandina volcano, Galápagos: The first circumferential dike intrusion observed by GPS and InSAR, *Bulletin of Volcanology*, *73*(6), 679-697. https://doi.org/10.1007/s00445-010-0433-0

Chen, C. W., and Zebker, H. A. (2000). Network approaches to two-dimensional phase unwrapping: intractability and two new algorithms, *Journal of the Optical Society of America A*, *17*(3), 401-414. https://doi.org/10.1364/JOSAA.17.000401

Corbi, F., Rivalta, E., Pinel, V., Maccaferri, F., Bagnardi, M., and Acocella, V. (2015). How caldera collapse shapes the shallow emplacement and transfer of magma in active volcanoes, *Earth and Planetary Science Letters*, *431*, 287-293. https://doi.org/10.1016/j.epsl.2015.09.028

Cullen, A., Vicenzi, E., and McBirney, A. R. (1989). Plagioclase-ultraphyric basalts of the Galapagos Archipelago, *Journal of Volcanology and Geothermal Research*, *37*(3-4), 325-337. https://doi.org/10.1016/0377-0273(89)90087-5

Davidge, L., Ebinger, C., Ruiz, M., Tepp, G., Amelung, F., Geist, D. et al. (2017). Seismicity patterns during a period of inflation at Sierra Negra volcano, Galápagos Ocean Island Chain, *Earth and Planetary Science Letters*, *462*, 169-179. https://doi.org/10.1016/j.epsl.2016.12.021

De Novellis, V., Castaldo, R., De Luca, C., Pepe, S., Zinno, I., Casu, F. et al. (2017). Source modelling of the 2015 Wolf volcano (Galápagos) eruption inferred from Sentinel 1-A DInSAR deformation maps and pre-eruptive ENVISAT time series, *Journal of Volcanology and Geothermal Research*, *344*, 246-256. https://doi.org/10.1016/j.jvolgeores.2017.05.013

Decriem, J., Árnadóttir, T., Hooper, A., Geirsson, H., Sigmundsson, F., Keiding, M. et al. (2010). The 2008 May 29 earthquake doublet in SW Iceland, *Geophysical Journal International*, *181*(2), 1128-1146. https://doi.org/10.1111/j.1365-246X.2010.04565.x

Farr, T. G., Rosen, P. A., Caro, E., Crippen, R., Duren, R., Hensley, S. et al. (2007). The shuttle radar topography mission, *Reviews of Geophysics*, *45*(2), RG2004. https://doi.org/10.1029/2005RG000183

Feighner, M. A., and Richards, M. A. (1994). Lithospheric structure and compensation mechanisms of the Galápagos Archipelago, *Journal of Geophysical Research: Solid Earth*, *99*(B4), 6711-6729. https://doi.org/10.1029/93JB03360

Geist, D., Howard, K. A., and Larson, P. (1995). The generation of oceanic rhyolites by crystal fractionation: the basalt-rhyolite association at Volcán Alcedo, Galápagos Archipelago, *Journal of Petrology*, *36*(4), 965-982. https://doi.org/10.1093/petrology/36.4.965

Geist, D., Naumann, T., and Larson, P. (1998). Evolution of Galápagos magmas: Mantle and crustal fractionation without assimilation, *Journal of Petrology*, *39*(5), 953-971. https://doi.org/10.1093/petroj/39.5.953

Geist, D., Diefenbach, B. A., Fornari, D. J., Kurz, M. D., Harpp, K., and Blusztajn, J. (2008a). Construction of the Galápagos platform by large submarine volcanic terraces, *Geochemistry, Geophysics, Geosystems*, *9*(3), Q03015. https://doi.org/10.1029/2007GC001795

Geist, D. J., Bergantz, G., and Chadwick Jr, W. W. (2014). Galápagos Magma Chambers. In K. S. Harpp, E. Mittelstaedt, N. d'Ozouville and D. W. Graham (Eds.), *The Galapagos: A natural laboratory for the Earth sciences*, *Geophysical Monograph Series* (Vol. 204, pp. 55-69). Washington, DC: American Geophysical Union.

Geist, D. J., Naumann, T. R., Standish, J. J., Kurz, M. D., Harpp, K. S., White, W. M., and Fornari, D. J. (2005). Wolf Volcano, Galápagos Archipelago: Melting and magmatic evolution at the margins of a mantle plume, *Journal of Petrology*, *46*(11), 2197-2224. https://doi.org/10.1093/petrology/egi052

Geist, D. J., Harpp, K. S., Naumann, T. R., Poland, M., Chadwick, W. W., Hall, M., and Rader, E. (2008b). The 2005 eruption of Sierra Negra volcano, Galápagos, Ecuador, *Bulletin of Volcanology*, *70*(6), 655-673. https://doi.org/10.1007/s00445-007-0160-3

González, P. J., Bagnardi, M., Hooper, A. J., Larsen, Y., Marinkovic, P., Samsonov, S. V., and Wright, T. J. (2015). The 2014–2015 eruption of Fogo volcano: Geodetic modeling of Sentinel- 1

TOPS interferometry, *Geophysical Research Letters*, *42*(21), 9239-9246. https://doi.org/10.1002/2015GL066003

Grove, T. L., Kinzler, R. J., and Bryan, W. B. (1992). Fractionation of mid- ocean ridge basalt (MORB). In J. P. Morgan, D. K. Blackman and J. M. Sinton (Eds.), *Mantle flow and melt generation at mid-ocean ridges*, *Geophysical Monograph Series* (Vol. 71, pp. 281-310). Washington, DC: American Geophysical Union.

Gudmundsson, M. T., Jónsdóttir, K., Hooper, A., Holohan, E. P., Halldórsson, S. A., Ófeigsson, B. G. et al. (2016). Gradual caldera collapse at Bárdarbunga volcano, Iceland, regulated by lateral magma outflow, *Science*, *353*(6296), aaf8988. https://doi.org/10.1126/science.aaf8988

Gudmundsson, O., Brandsdottir, B., Menke, W., and Sigvaldason, G. E. (1994). The crustal magma chamber of the Katla volcano in south Iceland revealed by 2-D seismic undershooting, *Geophysical Journal International*, *119*, 277-296. https://doi.org/10.1111/j.1365-246X.1994.tb00928.x

Halldórsson, S. A., Bali, E., Hartley, M. E., Neave, D. A., Peate, D. W., Guðfinnsson, G. H. et al. (2018). Petrology and geochemistry of the 2014–2015 Holuhraun eruption, central Iceland: compositional and mineralogical characteristics, temporal variability and magma storage, *Contributions to Mineralogy and Petrology*, *173*, 64. https://doi.org/10.1007/s00410-018-1487-9

Harpp, K. S., and Geist, D. J. (2018). The Evolution of Galápagos Volcanoes: An Alternative Perspective, *Frontiers in Earth Science*, *6*, 50. https://doi.org/10.3389/feart.2018.00050

Harpp, K. S., Mittelstaedt, E., d'Ozouville, N., and Graham, D. W. (Eds.). (2014). The Galápagos: A Natural Laboratory for the Earth Sciences. *Geophysical Monograph Series*. (Vol. 204). Washington, DC: American Geophysical Union.

Hartley, M. E., Bali, E., Maclennan, J., Neave, D. A., and Halldórsson, S. A. (2018). Melt inclusion constraints on petrogenesis of the 2014–2015 Holuhraun eruption, Iceland, *Contributions to Mineralogy and Petrology*, *173*, 10. https://doi.org/10.1007/s00410-017-1435-0

Hill, D. P., and Zucca, J. J. (1987). Geophysical constraints on the structure of Kilauea and Mauna Loa volcanoes and some implications for seismomagmatic processes. In R. W. Decker, T. L. Wright and P. H. Stauffer (Eds.), *Volcanism in Hawaii*, *Professional Paper 1350* (Vol. 2, pp. 903-917). Washington: U.S. Geological Survey.

Holness, M. B., Vukmanovic, Z., and Mariani, E. (2017a). Assessing the role of compaction in the formation of adcumulates: a microstructural perspective, *Journal of Petrology*, *58*(4), 643-673. https://doi.org/10.1093/petrology/egx037

Holness, M. B., Farr, R., and Neufeld, J. A. (2017b). Crystal settling and convection in the Shiant Isles Main Sill, *Contributions to Mineralogy and Petrology*, *172*, 7. https://doi.org/10.1007/s00410-016-1325-x

Holness, M. B., Anderson, A. T., Martin, V. M., Maclennan, J., Passmore, E., and Schwindinger, K. (2007). Textures in partially solidified crystalline nodules: a window into the pore structure of slowly cooled mafic intrusions, *Journal of Petrology*, *48*(7), 1243-1264. https://doi.org/10.1093/petrology/egm016

Hooper, A., Segall, P., and Zebker, H. (2007). Persistent scatterer interferometric synthetic aperture radar for crustal deformation analysis, with application to Volcán Alcedo, Galápagos, *Journal of Geophysical Research: Solid Earth*, *112*(B7), B07407. https://doi.org/10.1029/2006JB004763

Hooper, A., Zebker, H., Segall, P., and Kampes, B. (2004). A new method for measuring deformation on volcanoes and other natural terrains using InSAR persistent scatterers, *Geophysical Research Letters*, *31*(23), L23611. https://doi.org/10.1029/2004GL021737

Jarosewich, E., Nelen, J. A., and Norberg, J. A. (1980). Reference samples for electron microprobe analysis, *Geostandards and Geoanalytical Research*, *4*, 43-47. https://doi.org/10.1111/j.1751-908X.1980.tb00273.x

Jay, J., Costa, F., Pritchard, M., Lara, L., Singer, B., and Herrin, J. (2014). Locating magma reservoirs using InSAR and petrology before and during the 2011–2012 Cordón Caulle silicic eruption, *Earth and Planetary Science Letters*, *395*, 254-266. https://doi.org/10.1016/j.epsl.2014.03.046

Klügel, A., Longpré, M. A., García-Cañada, L., and Stix, J. (2015). Deep intrusions, lateral magma transport and related uplift at ocean island volcanoes, *Earth and Planetary Science Letters*, *431*, 140-149. https://doi.org/10.1016/j.epsl.2015.09.031

Kurz, M. D., and Geist, D. (1999). Dynamics of the Galapagos hotspot from helium isotope geochemistry, *Geochimica et Cosmochimica Acta*, *63*(23-24), 4139-4156. https://doi.org/10.1016/S0016-7037(99)00314-2

Laeger, K., Petrelli, M., Andronico, D., Misiti, V., Scarlato, P., Cimarelli, C. et al. (2017). High-resolution geochemistry of volcanic ash highlights complex magma dynamics during the Eyjafjallajökull 2010 eruption, *American Mineralogist*, *102*(6), 1173-1186. https://doi.org/10.2138/am-2017-5860

Longpré, M. A., Klügel, A., Diehl, A., and Stix, J. (2014). Mixing in mantle magma reservoirs prior to and during the 2011–2012 eruption at El Hierro, Canary Islands, *Geology*, *42*(4), 315-318. https://doi.org/10.1130/G35165.1

Maclennan, J., McKenzie, D. M., Gronvöld, K., and Slater, L. (2001). Crustal accretion under northern Iceland, *Earth and Planetary Science Letters*, *191*(3-4), 295-310. https://doi.org/10.1016/S0012-821X(01)00420-4

Magee, C., Stevenson, C. T. E., Ebmeier, S. K., Keir, D., Hammond, J. O. S., Gottsmann, J. H. et al. (2018). Magma Plumbing Systems: A Geophysical Perspective, *Journal of Petrology*, egy064. https://doi.org/10.1093/petrology/egy064

Marsh, B. D. (1996). Solidification fronts and magmatic evolution, *Mineralogical Magazine*, *60*(398), 5-40. https://doi.org/10.1180/minmag.1996.060.398.03

McBirney, A. R., and Williams, H. (Eds.). (1969). Geology and petrology of the Galapagos Islands. *Geological Society of America Memoir*. (Vol. 118).

McCormick Kilbride, B., Edmonds, M., and Biggs, J. (2016). Observing eruptions of gas-rich compressible magmas from space, *Nature Communications*, *7*, 13744. https://doi.org/10.1038/ncomms13744

McTigue, D. F. (1987). Elastic stress and deformation near a finite spherical magma body: Resolution of the point source paradox, *Journal of Geophysical Research: Solid Earth*, *92*(B12), 12931-12940. https://doi.org/10.1029/JB092iB12p12931

Mollo, S., Del Gaudio, P., Ventura, G., Iezzi, G., and Scarlato, P. (2010). Dependence of clinopyroxene composition on cooling rate in basaltic magmas: implications for thermobarometry, *Lithos*, *118*(3-4), 302-312. https://doi.org/10.1016/j.lithos.2010.05.006

Mollo, S., Putirka, K., Misiti, V., Soligo, M., and Scarlato, P. (2013). A new test for equilibrium based on clinopyroxene–melt pairs: Clues on the solidification temperatures of Etnean alkaline melts at post-eruptive conditions, *Chemical Geology*, *352*, 92-100. https://doi.org/10.1016/j.chemgeo.2013.05.026

Munro, D. C., and Rowland, S. K. (1996). Caldera morphology in the western Galapagos and implications for volcano eruptive behavior and mechanisms of caldera formation, *Journal of Volcanology and Geothermal Research*, *72*(1-2), 85-100. https://doi.org/10.1016/0377-0273(95)00076-3

Naumann, T., Geist, D., and Kurz, M. (2002). Petrology and geochemistry of Volcan Cerro Azul: Petrologic diversity among the western Galápagos volcanoes, *Journal of Petrology*, *43*(5), 859-883. https://doi.org/10.1093/petrology/43.5.859

Neave, D. A., and Putirka, K. D. (2017). A new clinopyroxene-liquid barometer, and implications for magma storage pressures under Icelandic rift zones, *American Mineralogist*, *102*(4), 777-794. https://doi.org/10.2138/am-2017-5968

Neave, D. A., Maclennan, J., Hartley, M. E., Edmonds, M., and Thordarson, T. (2014). Crystal storage and transfer in basaltic systems: the Skuggafjöll eruption, Iceland, *Journal of Petrology*, *55*(12), 2311-2346. https://doi.org/10.1093/petrology/egu058

Ofeigsson, B. G., Hooper, A., Sigmundsson, F., Sturkell, E., and Grapenthin, R. (2011). Deep magma storage at Hekla volcano, Iceland, revealed by InSAR time series analysis, *Journal of Geophysical Research: Solid Earth*, *116*(B5), B05401. https://doi.org/10.1029/2010JB007576

Okada, Y. (1985). Surface deformation due to shear and tensile faults in a half-space, *Bulletin of the seismological society of America*, *75*(4), 1135-1154.

Peterson, M. E., Kelley, K. A., Cottrell, E., Saal, A. E., and Kurz, M. D. (2015). *The oxidation state of Fe in glasses from the Galapagos Archipelago: Variable oxygen fugacity as a function of mantle source*. Paper presented at AGU Fall Meeting, San Francisco, CA.

Putirka, K. (1997). Magma transport at Hawaii: Inferences based on igneous thermobarometry, *Geology*, *25*(1), 69-72. https://doi.org/10.1130/0091-7613(1997)025<0069:MTAHIB>2.3.CO;2

Putirka, K. (1999). Clinopyroxene + liquid equilibria to 100 kbar and 2450 K, *Contributions to Mineralogy and Petrology*, *135*(2-3), 151-163. https://doi.org/10.1007/s004100050503

Putirka, K., Johnson, M., Kinzler, R., Longhi, J., and Walker, D. (1996). Thermobarometry of mafic igneous rocks based on clinopyroxene-liquid equilibria, 0–30 kbar, *Contributions to Mineralogy and Petrology*, *123*(1), 92-108. https://doi.org/10.1007/s004100050145

Putirka, K. D. (2008). Thermometers and barometers for volcanic systems, *Reviews in Mineralogy and Geochemistry*, *69*(1), 61-120. https://doi.org/10.2138/rmg.2008.69.3

Ridolfi, F., Renzulli, A., and Puerini, M. (2010). Stability and chemical equilibrium of amphibole in calc-alkaline magmas: an overview, new thermobarometric formulations and application to subduction-related volcanoes, *Contributions to Mineralogy and Petrology*, *160*(1), 45-66. https://doi.org/10.1007/s00410-009-0465-7

Rosen, P. A., Gurrola, E. M., Agram, P. S., Sacco, G. F., and Lavalle, M. (2015). *The InSAR Scientific Computing Environment (ISCE): A python framework for Earth science*. Paper presented at AGU Fall Meeting, San Francisco, CA.

Rudge, J. F. (2008). Finding peaks in geochemical distributions: A re-examination of the helium-continental crust correlation, *Earth and Planetary Science Letters*, *274*(1-2), 179-188. https://doi.org/10.1016/j.epsl.2008.07.021

Sheather, S. J., and Jones, M. C. (1991). A reliable data-based bandwidth selection method for kernel density estimation, *Journal of the Royal Statistical Society. Series B (Methodological)*, *53*(3), 683-690.

Siebert, L., Simkin, T., and Kimberly, P. (Eds.). (2011). *Volcanoes of the World*. Oakland, CA: University of California Press.

Sinton, C. W., Christie, D. M., Coombs, V. L., Nielsen, R. L., and Fisk, M. R. (1993). Near-primary melt inclusions in anorthite phenocrysts from the Galapagos Platfrom, *Earth and Planetary Science Letters*, *119*(4), 527-537. https://doi.org/10.1016/0012-821X(93)90060-M

Sliwinski, J. T., Bachmann, O., Ellis, B. S., Dávila-Harris, P., Nelson, B. K., and Dufek, J. (2015). Eruption of shallow crystal cumulates during explosive phonolitic eruptions on Tenerife, Canary Islands, *Journal of Petrology*, *56*(11), 2173-2194. https://doi.org/10.1093/petrology/egv068

Stock, M. J., Taylor, R. N., and Gernon, T. M. (2012). Triggering of major eruptions recorded by actively forming cumulates, *Scientific Reports*, *2*, 731. https://doi.org/10.1038/srep00731

Stock, M. J., Humphreys, M. C. S., Smith, V. C., Isaia, R., Brooker, R. A., and Pyle, D. M. (2018). Tracking volatile behaviour in sub-volcanic plumbing systems using apatite and glass: insights into pre-eruptive processes at Campi Flegrei, Italy, *Journal of Petrology*, egy020. https://doi.org/10.1093/petrology/egy020

Streck, M. J. (2008). Mineral textures and zoning as evidence for open system processes, *Reviews in Mineralogy and Geochemistry*, *69*(1), 595-622. https://doi.org/10.2138/rmg.2008.69.15

Tepp, G., Ebinger, C. J., Ruiz, M., and Belachew, M. (2014). Imaging rapidly deforming ocean island volcanoes in the western Galápagos archipelago, Ecuador, *Journal of Geophysical Research: Solid Earth*, *119*(1), 442-463. https://doi.org/10.1002/2013JB010227

Thomson, A., and Maclennan, J. (2012). The distribution of olivine compositions in Icelandic basalts and picrites, *Journal of Petrology*, *54*(4), 745-768. https://doi.org/10.1093/petrology/egs083

Ubide, T., and Kamber, B. S. (2018). Volcanic crystals as time capsules of eruption history, *Nature Communications*, *9*, 326. https://doi.org/10.1038/s41467-017-02274-w

Villagómez, D. R., Toomey, D. R., Hooft, E. E. E., and Solomon, S. C. (2011). Crustal structure beneath the Galápagos Archipelago from ambient noise tomography and its implications for plume-lithosphere interactions, *Journal of Geophysical Research: Solid Earth*, *116*, B04310. https://doi.org/10.1029/2010JB007764

Villagómez, D. R., Toomey, D. R., Geist, D. J., Hooft, E. E. E., and Solomon, S. C. (2014). Mantle flow and multistage melting beneath the Galápagos hotspot revealed by seismic imaging, *Nature Geoscience*, *7*, 151-156. https://doi.org/10.1038/ngeo2062

Voigt, M., Coogan, L. A., and von der Handt, A. (2017). Experimental investigation of the stability of clinopyroxene in mid-ocean ridge basalts: The role of Cr and Ca/Al, *Lithos*, *274-275*, 240-253. https://doi.org/10.1016/j.lithos.2017.01.003

Welsch, B., Hammer, J., Baronnet, A., Jacob, S., Hellebrand, E., and Sinton, J. (2016). Clinopyroxene in postshield Haleakala ankaramite: 2. Texture, compositional zoning and supersaturation in the magma, *Contributions to Mineralogy and Petrology*, *171*, 6. https://doi.org/10.1007/s00410-015-1213-9

Wilson, D. S., and Hey, R. N. (1995). History of rift propagation and magnetization intensity for the Cocos- Nazca spreading center, *Journal of Geophysical Research: Solid Earth*, *100*(B6), 10041-10056. https://doi.org/10.1029/95JB00762

Winpenny, B., and Maclennan, J. (2011). A partial record of mixing of mantle melts preserved in Icelandic phenocrysts, *Journal of Petrology*, *52*(9), 1791-1812. https://doi.org/10.1093/petrology/egr031

Xu, W., Jónsson, S., Ruch, J., and Aoki, Y. (2016). The 2015 Wolf volcano (Galápagos) eruption studied using Sentinel- 1 and ALOS- 2 data, *Geophysical Research Letters*, *43*(18), 9573-9580. https://doi.org/10.1002/2016GL069820

Yang, H. J., Kinzler, R. J., and Grove, T. L. (1996). Experiments and models of anhydrous, basaltic olivine-plagioclase-augite saturated melts from 0.001 to 10 kbar, *Contributions to Mineralogy and Petrology*, *124*(1), 1-18. https://doi.org/10.1007/s004100050169

Yun, S., Segall, P., and Zebker, H. (2006). Constraints on magma chamber geometry at Sierra Negra Volcano, Galápagos Islands, based on InSAR observations, *Journal of Volcanology and geothermal research*, *150*(1-3), 232-243. https://doi.org/10.1016/j.jvolgeores.2005.07.009

Figures

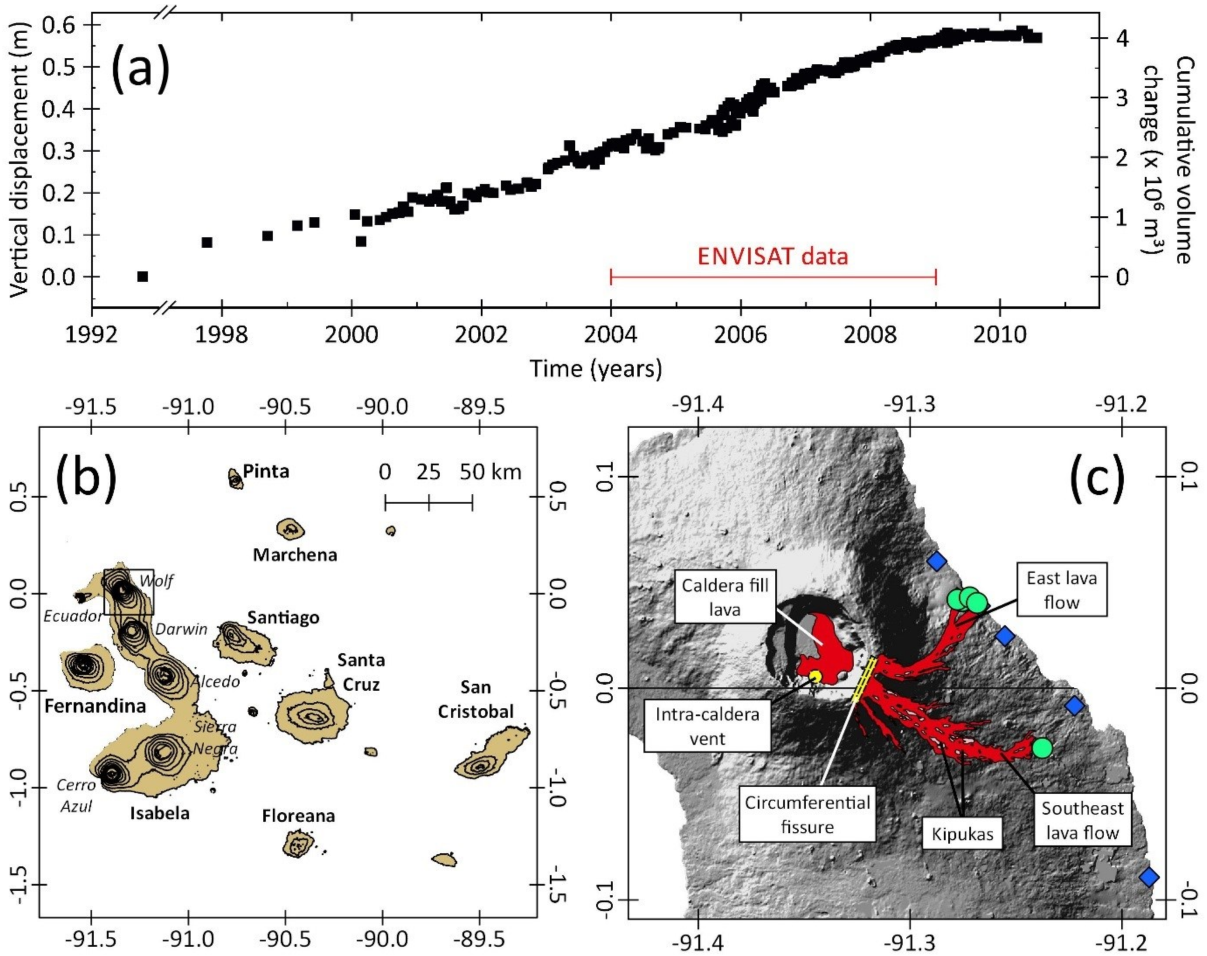

Figure 1: a) Time-series of ground deformation at Wolf volcano from the onset of SAR data collection (1992) to late-2010 when there was a pause in routine InSAR coverage, from *Bagnardi* [2014]. The red bar shows the period of ENVISAT data collection used to constrain the depth of the shallow deformation source. **b**) Regional map of the Galápagos Archipelago showing the different volcanic centres on Isabela Island (200 m contours). **c**) Detailed map of Wolf volcano. The 2015 lava flows are coloured red, with kipukas in pink, and the locations of the circumferential fissure and inra-caldera vent in yellow [after *Bernard et al.*, 2015]. Green circles and blue diamond's show sampling locations of lava and tephra samples used in this study, respectively.

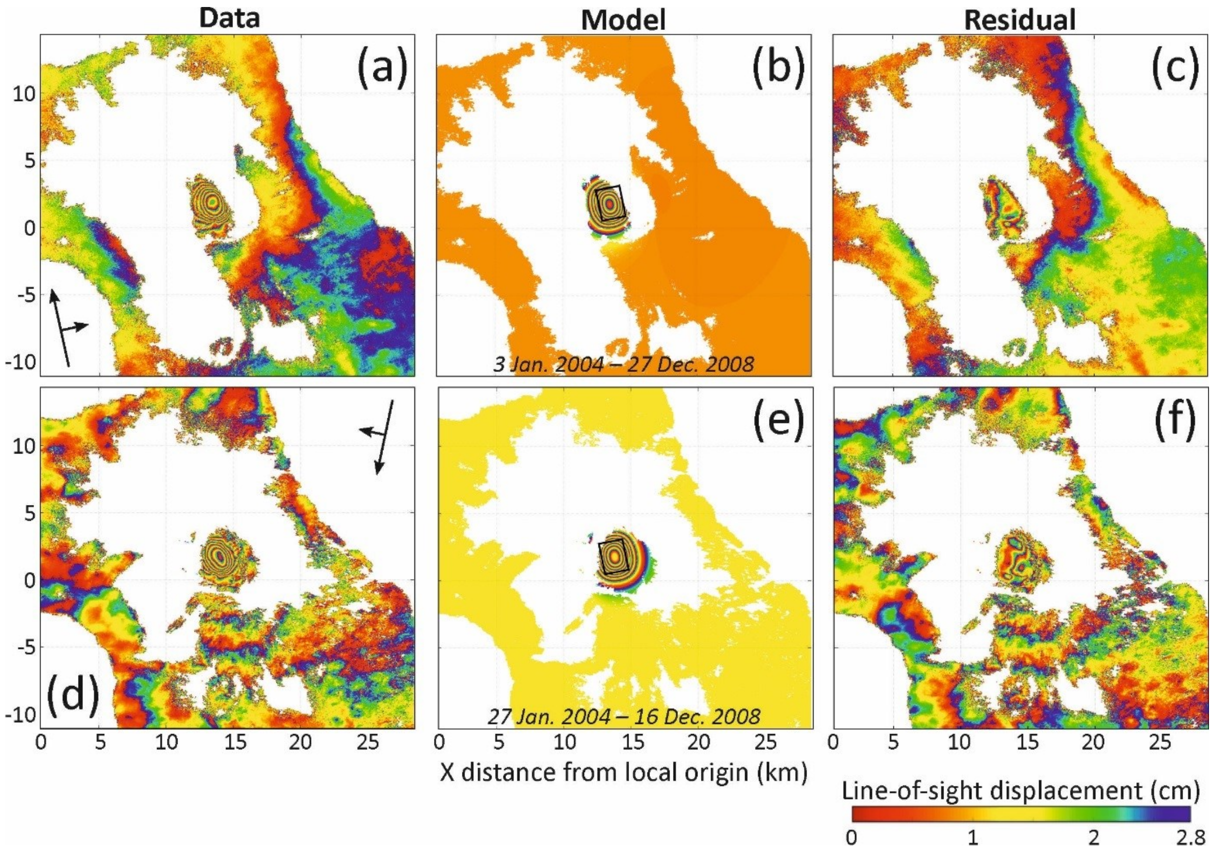

Figure 2: (left column; **a,d**) Envisat cumulative displacement maps (January 2004 – December 2008); (middle column; **b,e**) forward model using the maximum *a posteriori* probability solution; and (right column; **c,f**) residual maps. Black arrows show the flight direction of the satellite and the look direction. The black rectangle on model plots represents the outline of the optimal source solution. Each colour cycle (fringe) corresponds to 2.8 cm of displacement in the line-of-sight direction between the ground and the satellite.

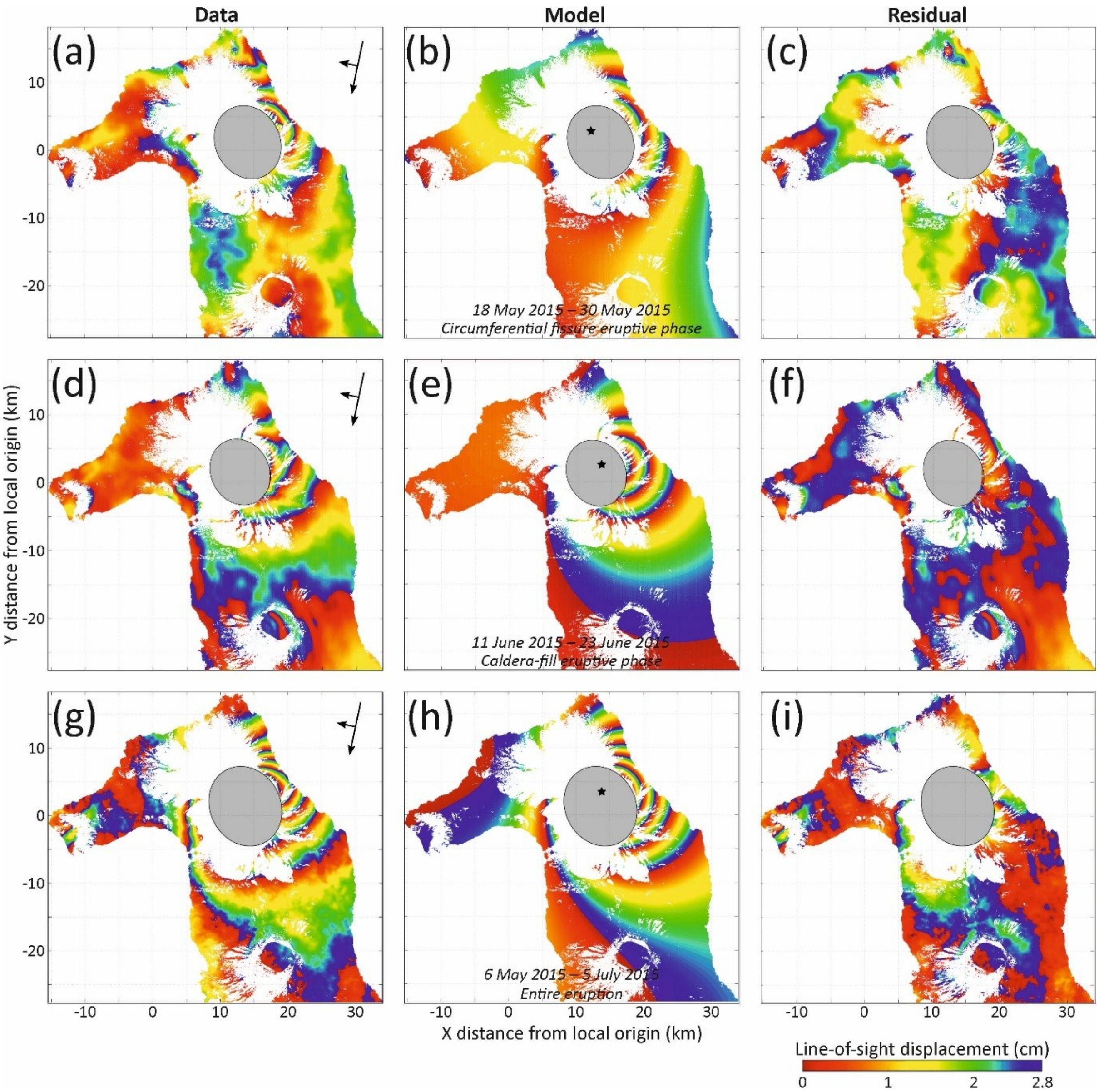

Figure 3: (left column; **a,d,g**) Sentinel-1 interferograms spanning the 2015 eruption at Wolf; (middle column; **b,e,h**) forward models using the maximum *a posteriori* probability solutions; and (right column; **c,f,i**) residual maps. Black arrows show the flight direction of the satellite and the look direction. The grey ellipses outline the areas masked before inversions. The black stars on model plots represent the source centroid location of the optimal source solutions. Each colour cycle (fringe) corresponds to 2.8 cm of displacement in the line-of-sight direction between the ground and the satellite.

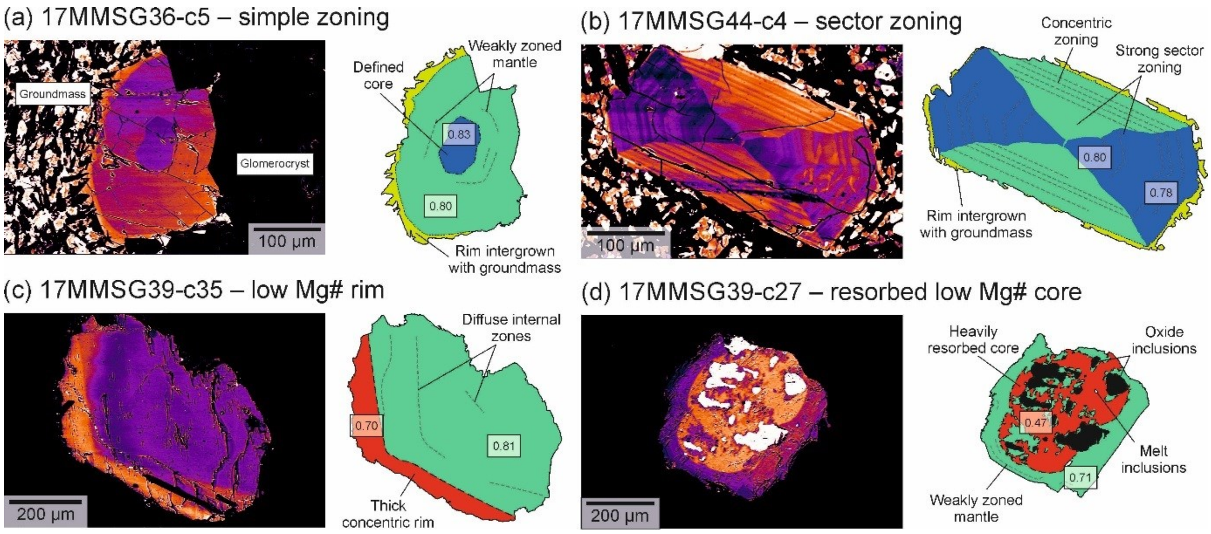

Figure 4: False-coloured BSE images showing macrocrystic clinopyroxene zoning textures in samples from the 2015 Wolf eruption. **a,b**) Crystals from lava samples showing simple core-rim zoning and sector zoning, respectively. Groundmass and glomerocryst material are labelled in (**a**), where they touch different sides of the crystal. **c,d**) Crystals from tephra samples that have a defined rim zone and heavily resorbed core, respectively. Annotated sketches of the different crystals are shown next to the BSE images to highlight the different zoning patterns. Numbers show representative Mg# in distinct parts of the crystals.

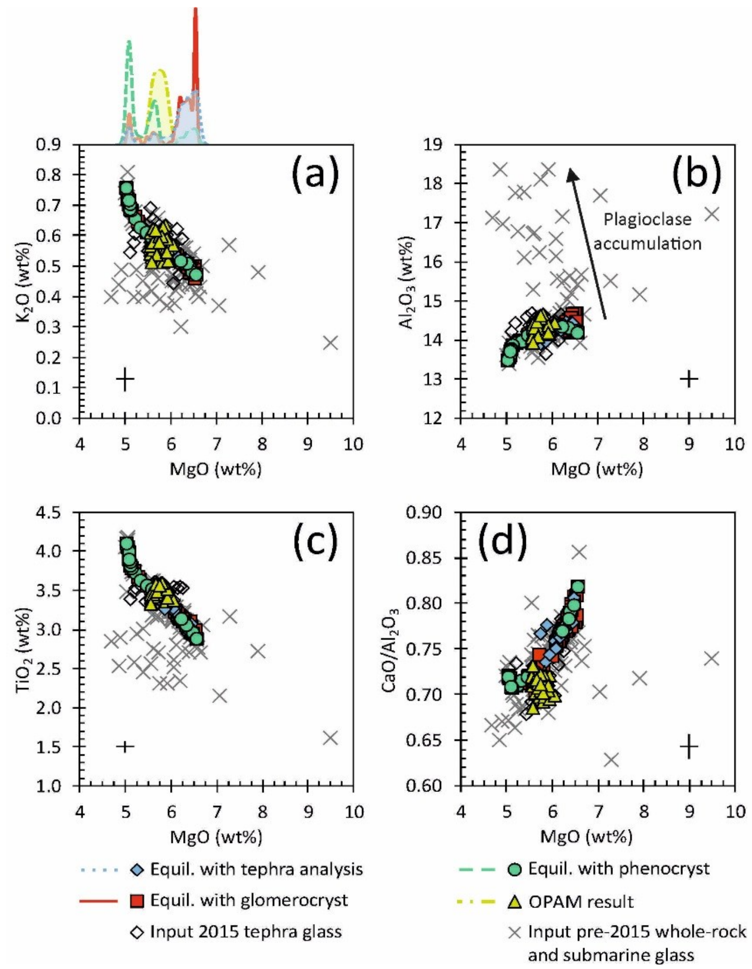

Figure 5: Glass and whole-rock compositions from Wolf volcano. Tephra glass compositions from the 2015 eruption (this study) and pre-2015 whole rock and submarine glass compositions [*Geist et al.*, 2005] used as inputs for barometric modelling are shown as black open diamonds and grey crosses, respectively. Filled symbols show the mean liquid compositions in equilibrium with clinopyroxene crystals in tephra samples (blue diamonds) and clinopyroxene phenocrysts (green circles) and glomerocrysts (red squares) in lava samples. Yellow diamonds show tephra glass compositions that returned P_F >0.8 and were used for OPAM modelling. The KDE above (**a**) shows the probability distribution of liquid MgO concentrations used for clinopyroxene-melt (blue dotted line, tephra crystals; green dashed line, lava phenocrysts; red solid line, lava glomerocrysts) and OPAM barometry (yellow dot-dashed line). The arrow in (**b**) shows the trajectory of whole-rock compositions affected by plagioclase accumulation – these did not return high P_F values or equilibrium matches with clinopyroxene crystals and were therefore not used for barometric modelling. Characteristic 2σ tephra glass EPMA uncertainties are shown.

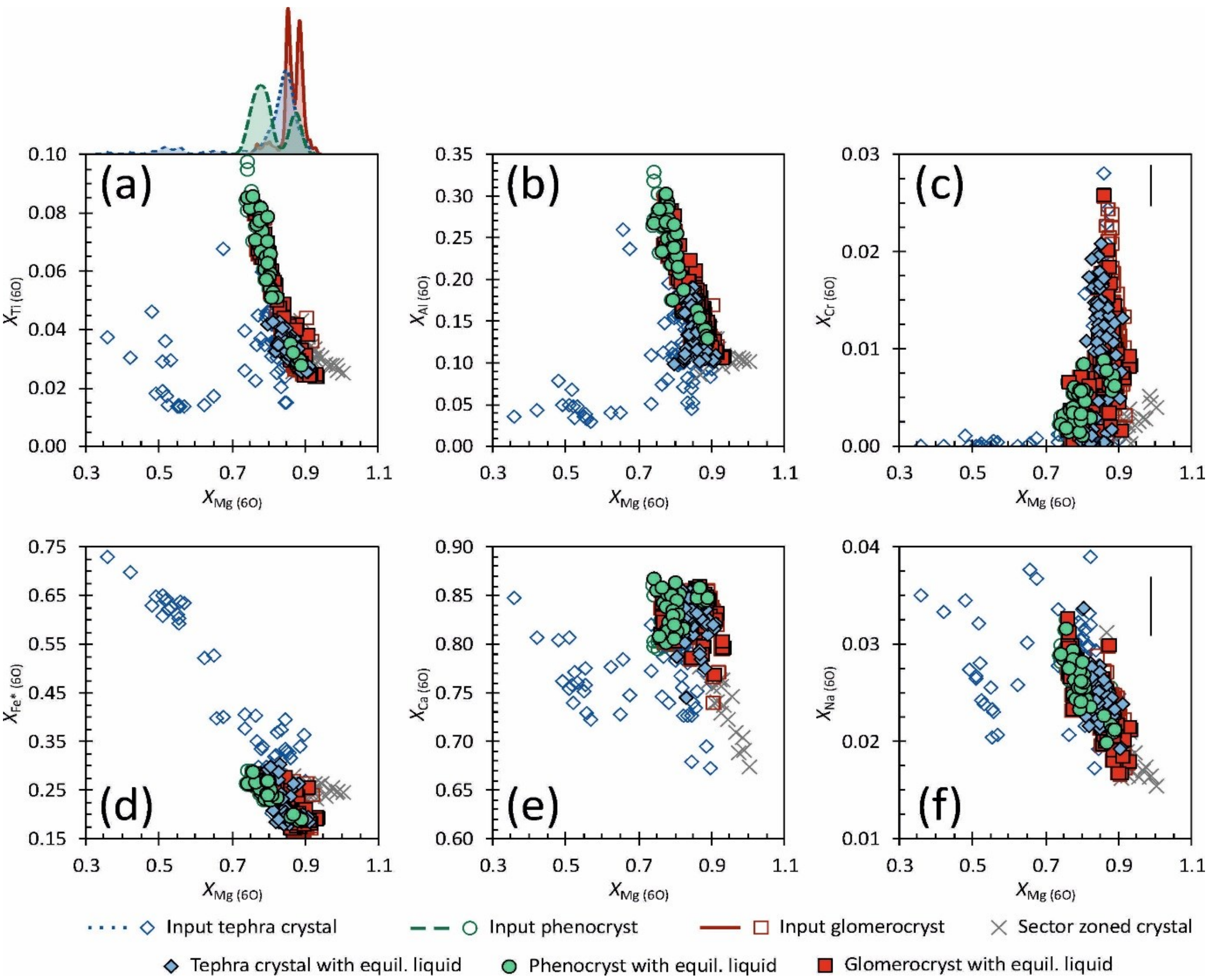

Figure 6: Clinopyroxene compositions from the 2015 Wolf eruption. Open symbols show all clinopyroxene analyses input into the equilibrium clinopyroxene-liquid matching algorithm. Filled symbols show clinopyroxene analyses that are in equilibrium with one or more input liquids (Fig. 5) and were used in clinopyroxene-melt barometry. Blue diamonds, green circles and red squares distinguish clinopyroxene analyses from tephra samples, clinopyroxene phenocrysts from lava samples and clinopyroxene glomerocrysts from lava samples, respectively. The KDE above (**a**) shows the probability distribution of clinopyroxene X_{Mg} contents in all measured crystals from tephra samples (blue dotted line), phenocrysts (green dashed line) and glomerocrysts (red solid line). The grey crosses are from a compositionally distinct sector zoned crystal (Fig. 1b), which grew under disequilibrium conditions and was not used for clinopyroxene-melt barometry. Crystal compositions were calculated on a 6O basis. Fe* = total FeO + Fe_2O_3. Characteristic 2σ analytical uncertainties are shown or are less than the size of a data point.

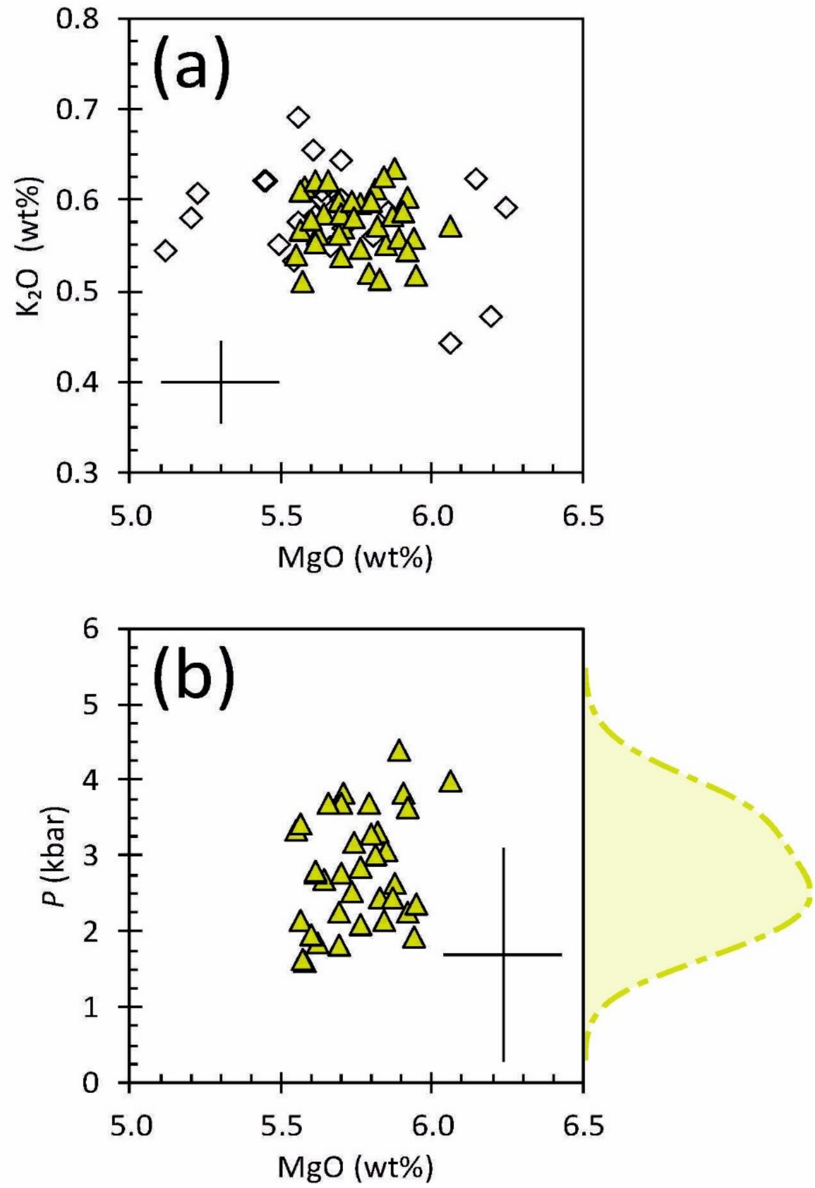

Figure 7: Pressure (*P*) estimates from 2015 Wolf eruption tephra glass analyses, calculated using the OPAM barometer of *Voigt et al.* [2017]. **a**) The compositions of all glass analyses measured in this study. Open diamonds returned P_F <0.8 and were not used for OPAM modelling. Filled yellow triangles returned P_F >0.8 and were used for OPAM barometry. **b**) Equilibration pressures calculated using the OPAM barometer. The KDE to the right of (**b**) shows the probability distribution of the calculated equilibration pressures. Error bars show characteristic 2σ analytical uncertainties for glass compositions and the SEE for the calculated pressures (1.4 kbar).

1001

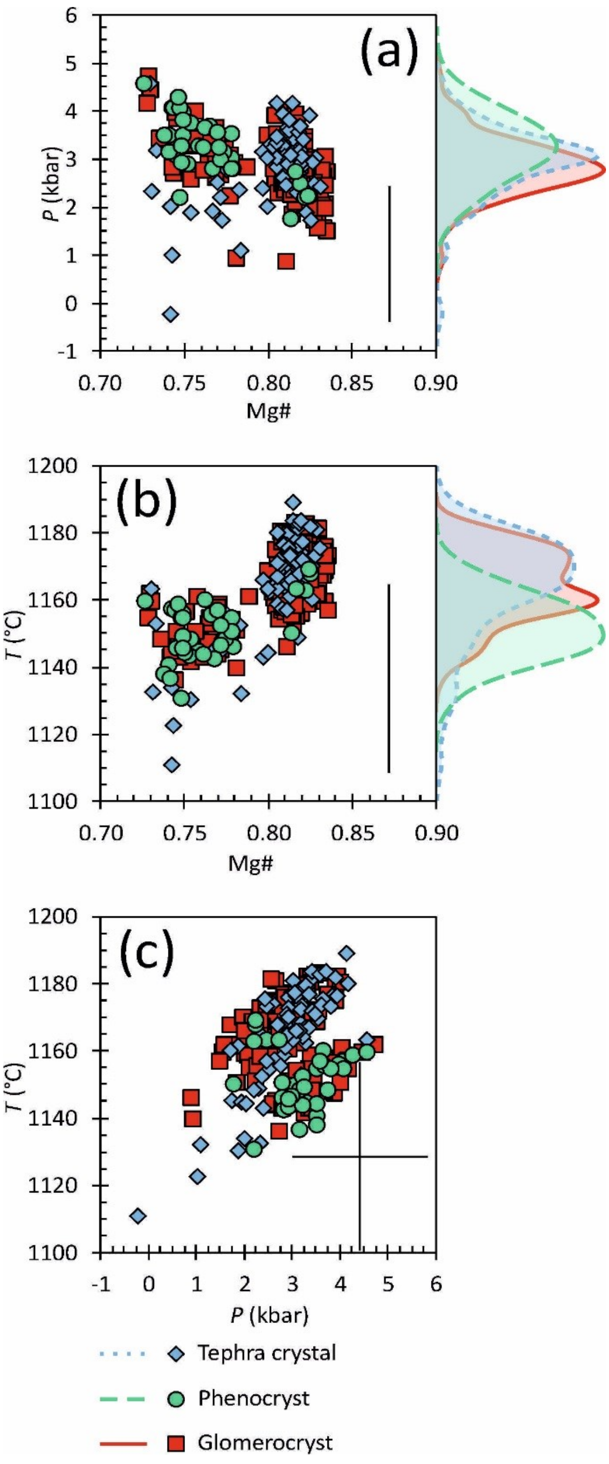

1002 **Figure 8:** Pressure (*P*) and temperature (*T*) estimates from 2015 Wolf eruption clinopyroxene
1003 analyses that are in equilibrium with one or more input liquids (Fig. 5), calculated using equation 1 of
1004 *Neave and Putirka* [2017] and equation 33 of *Putirka* [2008]. Panels (**a**) and (**b**) show clinopyroxene
1005 crystallisation *P* and *T* versus the crystal Mg# from the same analysis, respectively. Panel (**c**) shows
1006 clinopyroxene crystallisation *P* versus *T*. Blue diamonds, green circles and red squares distinguish

clinopyroxene analyses from tephra samples, clinopyroxene phenocrysts from lava samples and clinopyroxene glomerocrysts from lava samples, respectively. The KDEs to the right of panels (**a**) and (**b**) show the probability distribution of the calculated crystallisation *P* (**a**) and *T* (**b**) for clinopyroxene crystals in tephra samples (blue short-dashed line), phenocrysts from lava samples (green long-dashed line) and glomerocrysts from lava samples (red solid line). Standard error of estimates for the calculated pressures (1.4 kbar) and temperatures (28 °C) are shown. The Mg# uncertainty is less than the size of a data point.

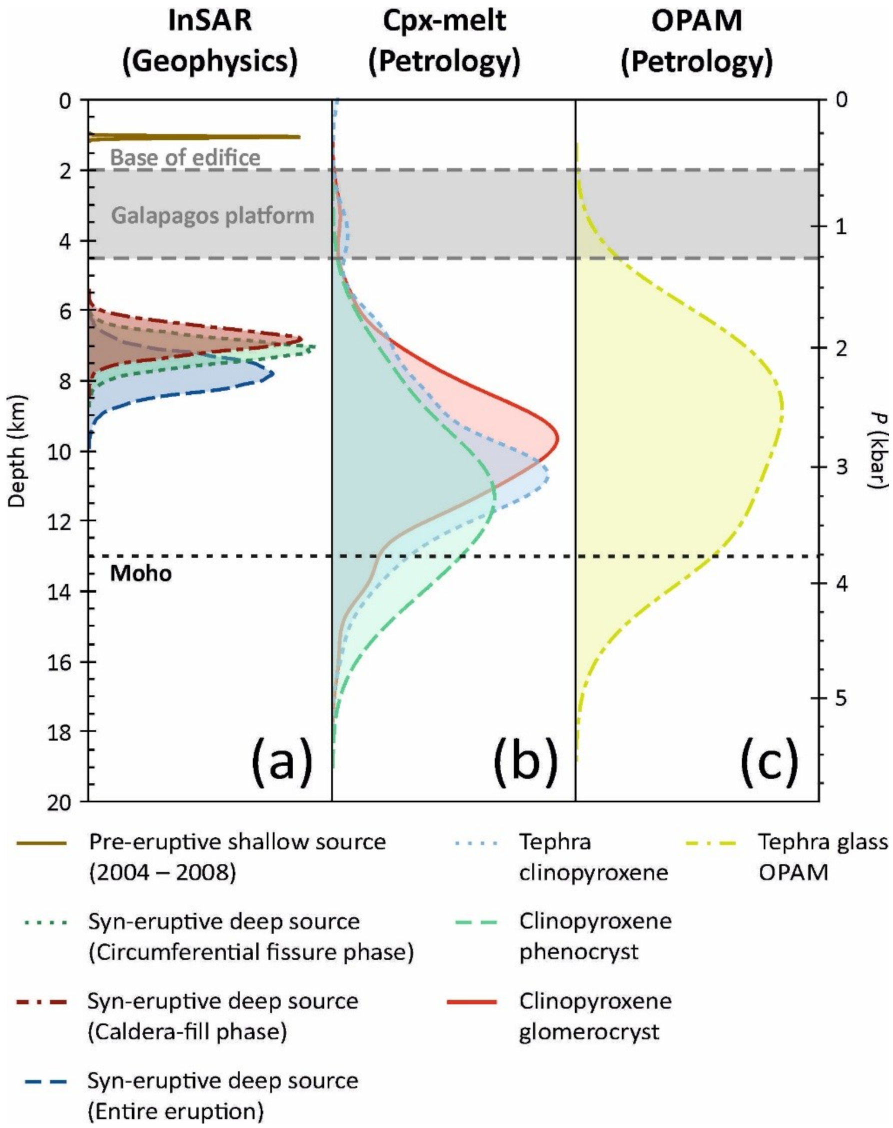

Figure 9: Comparison of magma storage depths at Wolf volcano determined using geophysical and petrological techniques. **a**) Normalised posterior probability distributions for the depths of Wolf deformation sources. The shallow source (dark yellow solid line) was constrained from pre-eruptive inflation and the deep source was constrained from syn-eruptive deflation during the circumferential fissure eruptive phase (dark green dotted line), caldera-fill eruptive phase (dark red dot-dashed line) and through the entire eruption (dark blue dashed line). **b**) Kernel density estimates showing the probability distribution of clinopyroxene crystallisation depths from clinopyroxene-melt barometry [*Neave and Putirka*, 2017]. The light blue dotted line, light green dashed line and light red solid line distinguish depths derived from clinopyroxene crystals in tephra samples, clinopyroxene phenocrysts in lava samples and clinopyroxene glomerocrysts from lava samples, respectively. **c**) Kernel density

estimate showing tephra glass equilibration depths from OPAM barometry [light yellow dot-dashed line; *Voigt et al.*, 2017]. The depths of the Moho [black dotted line; *Feighner and Richards*, 1994] and Galápagos platform [grey box; *Geist et al.*, 2008a] are shown for comparison. All depths are measured relative to the surface and petrological pressures were converted to depth using the polynomial depth vs pressure curve of *Putirka* [1997].

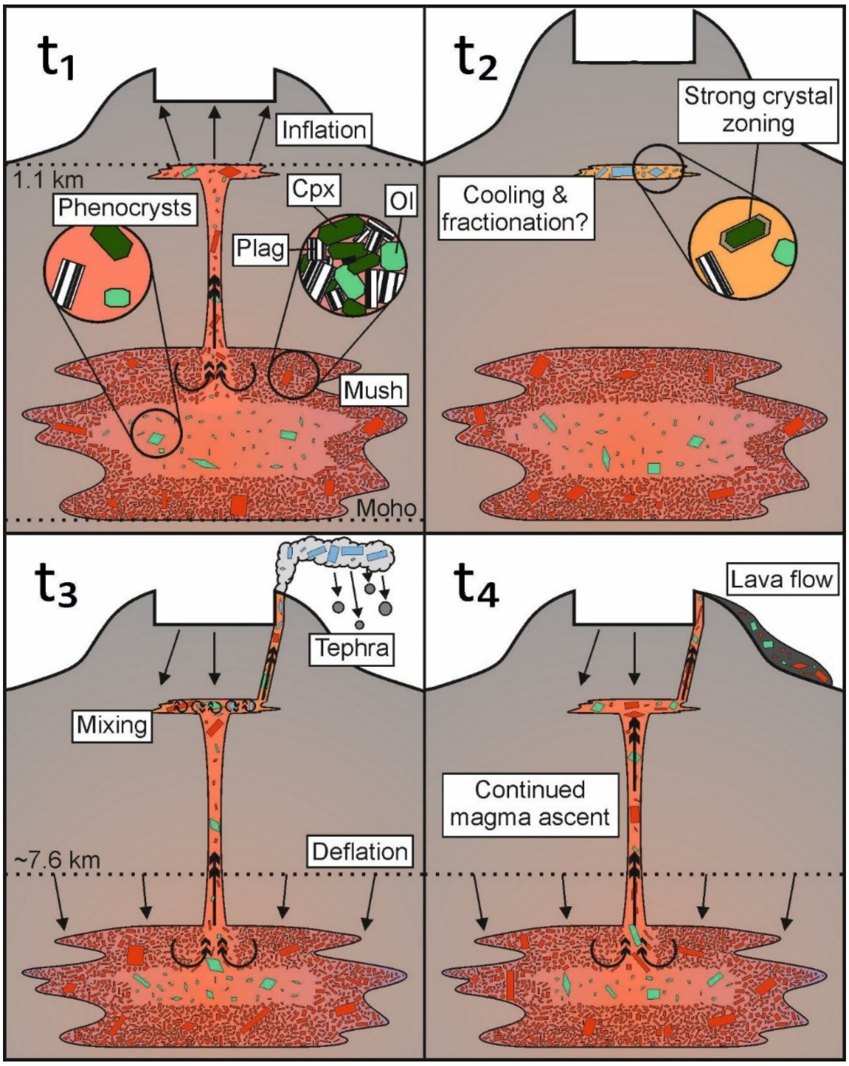

Figure 10: Schematic diagram summarising the architecture of the Wolf magma plumbing system before and during the 2015 eruption, constrained by our observations (not to scale). t_1–t_4 denote a relative time progression. Crystal colours represent crystals in tephra samples (blue), phenocrysts in lava samples (green) and glomerocrysts in lava samples (red). Ol, olivine; Plag, plagioclase; Cpx, clinopyroxene. **t_1**) Pre-eruptive inflation of a thin, shallow sill at 1.1 km by melts ascending from depth. The earliest measured deformation was between 1992–1997, with continuous inflation from 2000–2009. **t_2**) Hiatus in deformation beginning in 2009, representing a pause in magma ascent into the shallow sill. The shallow system is inferred to cool and fractionate during such pauses in magma recharge, leading to diverse crystal zoning patterns. **t_3**) Explosion during initiation of the 2015 eruption. Erupted melts equilibrated at depth (i.e. from OPAM barometry) but tephra glasses are heterogeneous, indicating some pre-eruptive magma mixing, likely within the shallow sill during

ascent. Tephra samples have a mixed clinopyroxene crystal cargo, including evolved crystals, inferred to be sourced from the shallow system, and more mafic (i.e. higher X_{Mg}) crystals sourced from depth. Both the shallow and deep magma storage regions show syn-eruptive deflation, with the deep source at ~7.6 km. $\mathbf{t_4}$) Eruption of lava flows from the circumferential fissure. Clinopyroxenes are all sourced from the lower crust, and include crystals derived from a mush zone (glomerocrysts) and a liquid-rich region (phenocrysts).